Journal of The Electrochemical Society, **160** (6) F716-F730 (2013)
0013-4651/2013/160(6)/F716/15/$31.00 © The Electrochemical Society

Oxygen Evolution during Water Electrolysis from Thin Films Using Bimetallic Oxides of Ir-Pt and Ir-Ru

Justin M. Roller,[a,b,z] M. Josefina Arellano-Jiménez,[c] Rishabh Jain,[a,b,*] Haoran Yu,[b,d] C. Barry Carter,[a,d] and Radenka Maric[a,b,d,]**

[a]*Department of Materials Science and Engineering, University of Connecticut, Storrs, Connecticut 06269, USA*
[b]*Center for Clean Energy Engineering, University of Connecticut, Storrs, Connecticut 06269, USA*
[c]*Departamento de Materiales Metálicos y Cerámicos, Instituto de Investigaciones en Materiales, Universidad Nacional Autónoma de México, Mexico D.F. 04510, México*
[d]*Department of Chemical and Biomolecular Engineering, University of Connecticut, Storrs, Connecticut 06269, USA*

Catalysts are required for both the oxidation of water and the reduction of oxygen. Blended oxides of Ir and Ru are superior for water oxidation whereas mixtures of Pt and Ir perform better when both oxidation of water and reduction of oxygen are required on the same electrode. A strategy for rationing these elements is explored by the formation of a thin film using a dry, flame process. $Ir_xPt_{1-x}O_{2-y}$ and $Ir_xRu_{1-x}O_{2-y}$ were both deposited from the vapor phase, as thin films, onto substrates of glassy carbon, polypropylene, and quartz. Elemental analysis of the Ir-Pt electrode suggests a stoichiometry of $Ir_{0.56}Pt_{0.44}O_{2-y}$. Bulk diffraction of the film shows two separate phases consisting of Pt metal and IrO_2. The sample showed signs of spallation after 10 cycles when scanned between 1.2 and 1.7 V. A weak oxygen evolution current of 0.8–0.4 mA/mg was measured at 1.6 V. Elemental analysis of the Ru-Ir film suggests a ratio of $Ru_{0.41}Ir_{0.59}O_{2-y}$. Phases of a homogeneous solid-solution of IrO_2 and RuO_2 and to a lesser extent Ru metal are shown by bulk X-ray diffraction. An exceptional oxygen evolution current of 25–40 mA/cm^2 was observed for the $Ru_{0.41}Ir_{0.59}O_{2-y}$ sample corresponding to a normalized mass activity of 400 mA/mg.
 [DOI: 10.1149/2.121306jes]

Manuscript submitted February 18, 2013; revised manuscript received March 28, 2013. Published April 24, 2013. This was Paper 1536 presented at the Seattle, Washington, Meeting of the Society, May 6–10, 2012.

Water electrolysis and oxygen reduction by proton exchange membranes.— A proton exchange membrane (PEM) functions as a semi-permeable separator to allow the transport of protons, isolate chemical reactants, and create an electrical insulation between two electrodes. The most commonly used PEM is Nafion, a DuPont product developed in the late 1960s as a permselective separator for chlor-alkali electrolyzers.[1] Nafion is formed by free radical initiated copolymerization of a crystallizable hydrophobic tetrafluoroethylene (TFE) backbone sequence with a co-monomer having pendant side chains of perfluorinated vinyl ethers terminated by perfluorosulfonic acid groups.[2]

PEM water electrolyzers (PEMWEs) utilize the PEM membrane, water, electrodes, and externally supplied electrons to pump protons up a chemical potential. The final products of acidic electrolysis are hydrogen on the cathode and oxygen on the anode. The overall chemical reaction, known as water splitting, is written as:

$$2H_2O(\ell) \rightarrow 2H_2(g) + O_2(g) \quad [1]$$

The hydrogen produced by a PEMWE, when powered by renewable sources of energy, provides a clean, efficient, energy carrier decoupled from the carbon cycle.[3–5] A PEM fuel cell (PEMFC) operates in reverse of a PEMWE in that oxygen and hydrogen are combined to produce water and electrons. When a PEMWE is combined at the systems level with a PEMFC the unit becomes capable of both energy conversion (fuel-cell mode) and energy storage (electrolysis mode). Two variants of the fuel cell and electrolyzer combination exist. In one embodiment, termed the unitized regenerative fuel cell (URFC), the electrochemical reactions for fuel cell and electrolyzer mode occur on the same electrode. An electrode capable of catalyzing the oxygen reduction reaction (ORR) and the oxygen evolution reaction (OER) is defined as a bifunctional oxygen electrode (BOE). In URFC systems, the oxygen and hydrogen electrodes function in both oxidation and reduction modes. The URFC integrates the fuel cell and electrolyzer units into a more compact configuration. Alternatively, the regenerative fuel cell (RFC) works by keeping the fuel cell and electrolyzer as separate units. A key advantage in using the URFC system is that water electrolysis and the hydrogen-oxygen recombination reactions occur on the same electrode to save valuable system real estate. The RFC consists of two separated subsystems: a fuel cell and an electrolyzer.[6] The benefit in using the RFC configuration is that each electrode can be optimized for only one reaction, i.e. reduction or oxidation.

A parallel exists between the charge-discharge modes in a secondary battery and the electrolyzer-fuel cell modes in a RFC or URFC. The charging analogy occurs when H_2 is produced via electrolysis and stored for future use. The discharging occurs when the H_2 is fed to the fuel cell and converted to direct current (DC) and water.

Oxygen evolution catalysis.— The rate-limiting step for water splitting is the activation of water at the anode for the OER which requires overpotentials above 1.23 V.[7] The sluggish kinetics of the OER requires the use of a noble metal electrocatalyst. In comparison, the overpotentials for H_2 evolution are much smaller.[8] The thermoneutral voltage, a state whereby no heat exchange occurs with the surroundings and all of the energy driving the electrolysis process comes from the electrical input energy, occurs at 1.48 V.[9] In order to generate appreciable current from water splitting, commercial electrolytic cells operate at voltages higher than thermoneutral. This excess potential generates heat that must be managed in the system design. In biological systems, oxygen-evolution catalysts fortunately avoid the use of rare noble metals and instead perform electrolysis with clusters of abundant transition metals such as Fe, Cu, Mo, Co, and Mn.[10] Oxygen evolution occurs during the photosynthetic respiration of plants using two protein complexes operating in series. During respiration, photo-excited electrons are transferred to enzymes and cofactors and these electrons must be replenished. This regeneration occurs in photosystem II by the oxidation of water to release electrons, hydrogen ions and molecular oxygen. Photosystem I then generates the reductant used in CO_2 reduction completing the respiration cycle.[11]

According to ab initio modeling by Rossmeisl et al.[12] and recent work by Suntivich et al.[13] the OER activity universally depends on the O_2 binding strength. Miles et al.[14] experimentally demonstrated that the electrocatalytic activity toward oxygen evolution in H_2SO_4 has a negative correlation with Pt content. Miles et al. found that Ru has the best activity. Alloys of RuIr, RuO_2 supported on TiO_2, and Ir each have a similar activity albeit lower than Ru. The performance drops further in alloys of IrPt followed by alloys of RuPt, and finally the catalyst with lowest OER activity is Pt. The type of acid has very little

*Electrochemical Society Student Member.
**Electrochemical Society Active Member.
[z]E-mail: Justin.roller@engr.uconn.edu

effect on the kinetic parameters. Furthermore, Miles et al. attributed the lower electrocatalytic activity in catalysts containing Pt catalysts to the formation of a deactivating PtO_2 film.

Oxides of Ir and Ru for electrolysis.— Driven largely by development of dimensionally stable anodes (DSAs) for the chlor-alkali industry, oxides of Ir and Ru have been used as catalysts on titanium substrates since the late 1960's.[15] Unfortunately, DSAs in PEMWEs are compromised by difficulty in obtaining a suitable contact between the electrocatalyst and the electrolyte.[16] Pt is the heritage catalyst typically used in PEMFCs. A successful catalyst must fully utilize the Pt without loss in performance or unwanted sacrifices in durability. Various methodologies have been developed to reduce the Pt mass loading (mg_{Pt}/cm^2) in PEMFC systems.[17] Dispersion of the catalyst onto high surface area carbon supports, alloying, and formation of core-shell structures have all been used with various degrees of success.[18–22] While Pt is a good catalyst for oxygen reduction it is poor for oxygen evolution and is not stable at the high OER potentials used in acidic water electrolysis.[16,23] Ir increases the activity and stability of Pt as a BOE in URFCs both in oxygen reduction and oxygen evolution modes.[24]

Dispersion of the catalyst onto a support as a strategy to reduce precious metal use is not possible on the carbon dispersants used in PEMFCs since carbon combustion occurs under the strong oxidizing conditions (pure O_2) in acidic environments (i.e. 0.5 M H_2SO_4).

$$C + H_2O \rightarrow CO_2 + 4H^+ + 4e^- 0.96\,V\,vs\,RHE \qquad [2]$$

Ru exhibits the best onset potential toward water activation but forms a film of RuO_2 during anodic polarization.[25] This hydrated oxide film is unstable and eventually dissolves.[26,27] Bulk RuO_2 is more active near the thermoneutral voltage; however, corrosion again converts this species to the soluble, unstable RuO_4. Kotz and Stucki showed that even small amounts of IrO_2 (20%) reduce the corrosion rate to 4% of the original value.[28] Fortunately, Ir^{4+} forms a solid solution with the RuO_2 lattice. This solubility is due to a similar atomic radius between Ir^{4+} (0.077 nm) and Ru^{4+} (0.076 nm).[29] The IrO_2 performs a dual role by both increasing stability and reducing the overpotential compared to RuO_2.[23] McDaniel and Schneider[30] reported a continuous range of solid solubility for the RuO_2-IrO_2 system with the oxides stable up to 1020°C. This solubility occurs because both adopt a rutile-type structure. Dissolution occurs by substitution owing to the similar radii. Unusual to the bonding in most metal oxides, both Ir and Ru oxide exhibit a delocalization of the outer shell electrons that give rise to a metallic-type binding; the electrical conductivities in these metal oxides are some of the highest known.[31]

Oxygen evolution catalysts have also been employed in PEMFC cathodes to favor oxygen evolution over carbon corrosion,[22,32] a drawback in this approach is the difficulty in forming a porous layer so that additional mass transport resistances are avoided, and the cost incurred by Ir and Ru.[33] Ir is a platinum group metal, with a relative abundance in the earth's crust less than one tenth than that of Pt, and economics dictates a rationing approach similar to Pt in catalyst design.[34,35]

Catalyst film formation.— IrO_2 forms a solid solution with Ru or Pt, therefore a range of compositions can be expressed by noting the Ir elemental ratio by x ($0 \leq x \leq 1$) in the chemical formula.[14,36] Additionally, non-stoichiometry between the oxide and metallic forms is denoted by y, the oxygen deficiency. Methods to form films of $Ir_xRu_{1-x}O_{2-y}$ or $Ir_xPt_{1-x}O_{2-y}$ fall into two categories: direct or indirect. Direct, dry film formation (e.g., sputtering, chemical vapor deposition (CVD) or flame based processes such as reactive spray deposition technology (RSDT)) combines the synthesis and formation into one step. Indirect, wet-methods require powder synthesis (e.g., pyrolysis of chloride salts, hydrolysis, Adam's fusion, or microwave-assisted polyol process method) followed by an electrode-formation step (e.g., tape casting, ink spraying, or screen printing).[31,37–44] A variety of processing routes for producing thin films of transition metal oxides are available including CVD, Physical vapor deposition (PVD), and sputtering,[45] however, these direct, dry film-formation techniques are batch processes that require vacuum equipment which then drives up the capital costs.[46,47] Recent advances in high-throughput combinatorial studies have enabled the search for binary and ternary OER electrocatalysts made by an impregnation/freeze-drying and subsequent annealing step or reduction via $NaBH_4$.[48,49] Wet powder-methods require purification of the powder, slurry formation, film formation and subsequent drying. In order to avoid the added processing steps required by wet-powder methods and the use of inherently batch vacuum methods, our approach to thin-film formation is via the dry, direct and continuous RSDT technique.[37,38,50]

Regardless of the processing technique used, for film formation, the surface mixed oxides can form a homogeneous solid-solution whereby Ir and Ru are atomically mixed in the crystal lattice, they can be present as separate crystallites, or exist a combination of both.[44,51] It has been reported[43] that the film surface changes dramatically, from the "as-prepared" state, after voltage cycling due to oxidation and surface restructuring and that a significant amount of hydration occurs in the oxide layers.[51]

Flame synthesis technology.— In this work, oxides of $Ir_xRu_{1-x}O_{2-y}$ for electrolysis and $Ir_xPt_{1-x}O_2$ for oxygen reduction/evolution were prepared by using the direct, dry, jet-flame based process RSDT. RSDT has been used to make a wide array of material systems that include Pt, CeO_2, SnO_2, Sn-Pt, $LiCoO_2$, $Ir_xRu_{1-x}O_{2-y}$, $Gd_{0.2}Ce_{0.8}O_{1.9}$.[37,38,52–58] Some key advantages of the RSDT process, over traditional processing methods, are i) a reduction in the number of processing steps required for catalyst formation and electrode application, ii) avoidance of wet processing and the concomitant binders, iii) no drying cycles, iv) lack of requirement for vacuum, v) power consumption <2 kW, and vi) ease of stoichiometry control by solution-based mixing of the precursors.

Flame technology, of which RSDT is a subset, is best known for large-scale production of carbon black.[59] Global carbon black production is forecast to be 11.6 Mt/year in 2013 with 70% going to tires and 20% for rubber.[60] The other common powders produced by flame-based methods in large quantities include: titania (e.g., Degussa P25 TiO_2) produced at ~0.2 Mt/year for pigments; ZnO (0.6 Mt/year) as an activator for rubber vulcanization, pigment or pharmaceutical additive; and fumed silica (~0.2 Mt/year) as a powder flowing aid, cosmetics additive, and in fabrication of optical fibers for telecommunications.[61] Variants of the industrial process have been developed by many groups to make Al_2O_3, Fe_2O_3, $BaCO_3$, CeO_2, Pt, monoclinic Y_2O, and tetragonal ZrO_2 among others.[62–71] Since 2006, Maric et al. have used the RSDT variant of flame processing to reduce Pt loading in PEMFC catalysts by directly applying catalyst layers onto electrolyte substrates using a catalyst coated membrane (CCM) approach.[37,50,72–74] CCMs have significant benefits over gas diffusion electrode (GDE) based MEAs, including: improved contact between the catalyst layer and the electrolyte that reduces contact resistance, improved catalyst utilization, and better control of catalyst loading when using thinner catalyst layers or low loadings.[75]

Reactive spray deposition technology (RSDT).— The RSDT process combines catalyst production and electrode formation into one step, takes place in the open atmosphere and eliminates the need to dispose of solvent waste; the solvent is completely combusted to CO_2 and H_2O. Fig. 1 shows a diagram of the general process.

In the RSDT process, xylene has a dual role by acting both as a cheap solvent, and as a fuel; xylene releases its enthalpic heat of combustion to decompose the metal cations and hydrocarbon anions. $Ir_xRu_{1-x}O_{2-y}$ and $Ir_xPt_{1-x}O_2$ nanoparticles, formed by decomposition in the vapor phase, grow from acetylacetonate (i.e., 2, 4-pentanedionate) ligands of the requisite metal. Acetylacetonates, as a general class of metal-organic ligands, are ideally suited for RSDT since they are soluble in a combustible organic, and do not contain any halide or

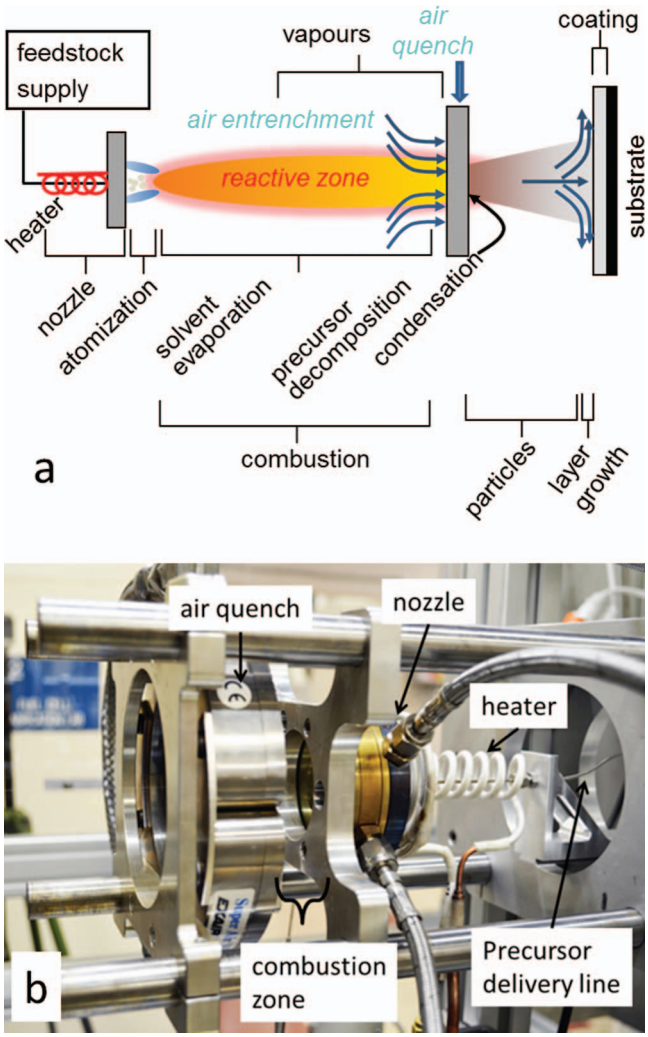

Figure 1. a) Abstract diagram of the RSDT process and b) a mirror image of the process as set-up for deposition, substrate not shown.

nitrate contaminants. The xylene is atomized and subsequently oxidized (i.e., combusted) into CO_2 and H_2O. To aid in atomization and to increase the heat released, 10–30 wt% of propane is added to the xylene. The droplet size produced by the RSDT nozzle is predominately sub-micron due to the simultaneous action of heat, pressure drop, and supercritical propane expansion. To ensure that nanoparticles of the desired product are formed, the metal-organic precursor must be confined to the nanoscale regime after droplet formation. This confinement condition limits growth during precipitation in the rapidly evaporating solvent.

Particle formation in flames.— Oxidation or reduction occurs according to the relative oxidizing strength of the flame, the activity of the metal species, and the partial pressures of CO_2 and H_2O. The oxidizing strength can be manipulated by the O_2 partial pressure in the combustion atmosphere,[76,77] and adjustments in the equivalence ratio.[78] The equivalence ratio, Φ, is the relationship between the stoichiometric oxidant and fuel molar flow rates divided by the actual process ratio; the relationship is expressed in equation 3.

$$\Phi = \frac{(\dot{n}_{oxidant}/\dot{n}_{fuel})_{stoic}}{(\dot{n}_{oxidant}/\dot{n}_{fuel})_{real}} \quad [3]$$

$\dot{n}$ is the molar flux (mol/s) of the oxidant or fuel. Equivalence ratios greater than 1 indicate a fuel rich mixture while ratios equal to 1 indicate a stoichiometric mixture of oxidant to fuel. When the equivalence ratio equals less than 1 the combustion mixture is oxidant rich. In this manuscript the flow rate of fuel (xylene) was kept constant at 32.7 millimole/min (4.0 mL/min) while the oxygen flow rate was set to 1,428 millimole/min (15,000 mL/min), giving an equivalence ratio of 0.27 indicating an oxidant rich flame. The equivalence ratio in the RSDT process is controlled by increasing or decreasing the oxygen supply to the atomization nozzle.

It is from the vapor phase that nucleation of the metal or metal oxide occurs along with growth of the primary particle along the length of the hot reactive zone.[79] There may be several pathways through which the vaporized metal reacts, nucleates, and grows either during time of flight or directly onto the substrate.[80] The precursor, once the droplet exits the nozzle, proceeds through the following steps: heats up to the boiling point of the solvent; precipitates due to a rapid solvent shell volume decrease (i.e., simultaneous evaporation and combustion); decomposes; phase changes from solid to vapor; and finally undergoes a series of redox reactions. Pt^{2+} is reduced to Pt metal while both Ru and Ir are oxidized from the (III) to (IV) states. Formation of the nanocrystallite particles, during time-of-flight, occurs prior to film formation through a multi-step process on a time scale of milliseconds. The general mechanism of particle growth, once the precursor has vaporized, occurs by: homogeneous reactions, nucleation, surface growth, cluster dynamics (a transitory state between single atoms and solid material), coalescence, aggregation, and agglomeration. The solid particle passes through the following size classifications during the growth process: monomer formation, cluster, primary particle, nanoparticle, and then agglomerate.[62–64] Depending on the processing conditions, a film can form either from the vapor phase (i.e., the product reaches the substrate at a stage somewhere between the monomer and nanoparticle pathway), by a physical impingement of a fully formed nanoparticle, or by a combination of both mechanisms.

The exact mechanism of growth is affected by the synthesis thermal profile, concentration of reactants, the precursor composition, oxidant/fuel flow rates, and the distance between the substrate and the nozzle. The thermal profile is controlled by the equivalence ratio, choice of fuel, quench distance, stand-off distance, flow rate, and nozzle design. Primary particle growth is arrested through rapid cooling by an air quench, to create a fast non-equilibrium phase change.[81] The time of flight, zone temperature profile, stand-off distance, and locations of the quench are critical to formation of the desired metal and morphology.[62]

Experimental

Precursor preparation.— Two different oxides; $Ir_xRu_{1-x}O_{2-y}$ for electrolysis and $Ir_xPt_{1-x}O_{2-y}$ for oxygen reduction/evolution; were prepared by dissolving either a i) 50:50 molar ratio of the metal organic solutes, Ru(III)-acetylacetonate, and Ir (III)-acetylacetonate or ii) a 50:50 platinum 2,4-pentanedionate and Ir (III)-acetylacetonate (Colonial Metals Inc.) into xylenes (Aldrich, ACS reagent ≥98.5%). The decomposition profile of Ir-acac and Ru-acac were studied by TGA in air at a rate of 5°C/min up to 550°C (TA Instruments, TGA-Q500). The solution was placed in a custom-made pressure vessel using a sanitary tee sight glass assembly with stainless cap plates (JCD54, Swagelok). The vessel was then capped; sealing was ensured by using a high pressure clamp torqued to 25 ft-lbs. Propane (Airgas, Industrial Grade) was added until a mass ratio of 15 wt% was obtained. The addition of propane brought the final metal concentrations to 1.4 mM each (i.e., 2.8 mM combined).

Reactive spray deposition technology system.— During deposition, the precursor solution was then pumped at a volumetric flow rate of 4 mL/min by an Isco 500D (Teledyne Isco, Lincoln NE) syringe pump through a custom-built atomizing nozzle. This flow rate was chosen to ensure adequate fuel atomization that matches the available power input, pressure drop through the nozzle, and flow capacity of the oxidant while ensuring no precursor is found on the substrates.

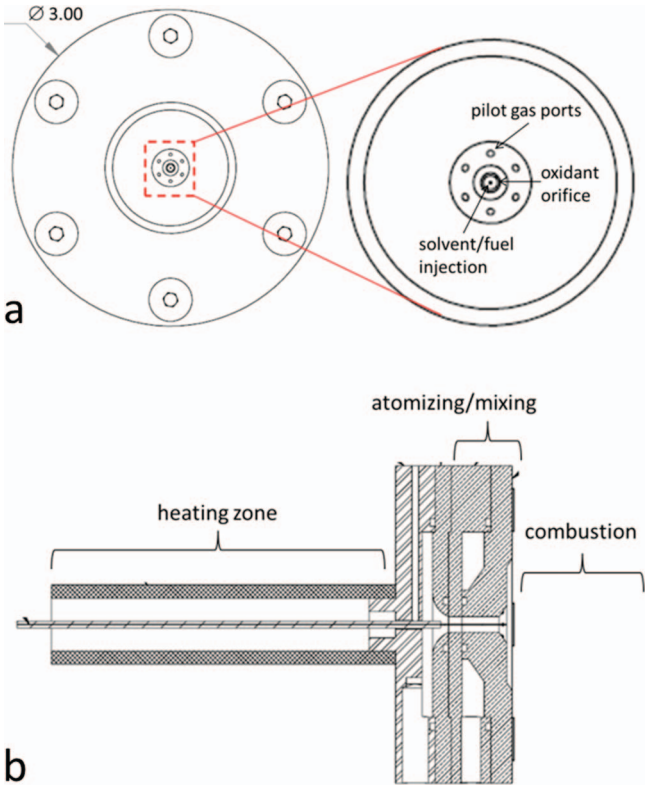

Figure 2. RSDT nozzle showing the a) injection geometry of the fuel/solvent, oxidant, and pilot gases and b) the three zones: heating, atomization/mixing, and combustion.

The nozzle consists of three stages, heating, atomizing/mixing, and combustion, as revealed in Fig. 2.

The heating stage consists of a 316 stainless steel tube (Cadence Science, Cranston RI) that has an outer diameter of 0.159 cm is 10 cm in length, and has an inner diameter of 0.25-1 mm. Soldered to the end of the tube was a 21–32 gauge hypodermic insert with a length of 1.8 cm and an inner diameter of 100–200 μm. The hypodermic insert acted as a restrictor to induce a fast pressure drop just prior to exit into the atomizing/mixing zone. The tube was heated by an EasyHeat 0112 (Ameritherm, Scottsville, NY) power supply using a custom coil. The control point for monitoring the process temperature was located 9.9 cm from the entry of the tube. Precursor solution was continuously passed through the heating stage at a flow rate 4 mL/min. The hypodermic insert was surrounded by a Ø 0.38 cm concentric channel for supplying oxygen as the fuel oxidant. The hypodermic insert was centered in the channel by a guide to maintain a centered position. Both insert and channel emptied their contents, using a co-flow geometry, into the open atmosphere. The precursor mixture exited the hypodermic insert housed in the body of the nozzle as a fine spray. The atomization of the precursor solution, generated by this nozzle, was formed by a combination of pressure, heat produced using the induction system, and supercritical atomization due to the expansion of the liquefied propane above its critical temperature of 96.6°C. The combined action of these energy inputs forms droplets less than 1 μm in diameter. In the atomizing/mixing stage, the oxygen and the fuel droplets (i.e. xylene-propane mixture) are turbulently mixed prior to ignition. This mixing, prior to ignition, classifies this type of combustion as a premixed flame; the conical shape of the flame tip denotes that the flame speed (i.e., rate of expansion of the flame front) is controlled by the fuel-oxidant flow and not the reaction chemistry. The length of the atomizing/mixing zone is 0.20–0.38 cm. The final stage of the nozzle was the ignition zone. This portion consists of six circular ports having a Ø 0.05 cm and angled at 45° to the centerline of the hypodermic needle. The six ports were evenly spaced on a 0.32–0.64 cm radius around the hypodermic insert. These ports supply a premixed methane and oxygen stream that was ignited to stabilize the high exit-velocity jet-flame formed by the custom nozzle.

After the ignition zone a circular air-quench (Exair, Cincinnati, OH), located 5–10 cm from the end of the hypodermic insert, was centered axially on the flame. The purpose of the air-quench was to dilute, with air at 25°C, the combustion zone and thus rapidly cool the flame zone. This has two distinct functions: it stops the particle growth and it allows a wider range of substrate materials to be positioned at lower stand-off distances. After passing through the quench, the luminosity of the flame is greatly diminished. The product stream consists of nanoparticles and aggregates that then impinge directly onto substrate(s) located at stand-off distances between 15–20 cm.

A custom made holder, shown in Fig. 3, was fabricated to simultaneously position three glassy carbon or gold rotating disk electrodes (RDE) (ACE6DC050GC and ACE6DC050AU, Pine Instruments) for direct application of a film without any binder. The electrode diameter is 0.5 cm creating an active area of 0.196 cm^2. The electrodes were placed into a polytetrafluoroethylene (PTFE) "U-cup" (AKUCUP, Pine Instruments) and pressed into the holder to prevent any deposition on the sides of the electrode, see Fig. 3. Another custom holder was also fabricated to affix: a polypropylene coupon, for elemental analysis by inductively coupled plasma optical emission spectroscopy ICP-OES; a Ø 2.54 cm quartz disk cut 6° from (0001) (Gem Dugout, State College PA), for phase identification by X-ray diffraction; and either an aluminum SEM pin stub specimen mount (16111, Ted Pella, Inc.) or a 6.45 cm^2 square by 2 mm thick glassy (vitreous) carbon plate for electron imaging. A third holder, to allow for fast removal of Cu grids during a deposition, held meshed grids coated with either; ultrathin carbon (<3 nm) on a holey carbon support film (300 mesh) or lacey formvar stabilized with carbon (200 mesh) (Ted Pella, 01824 and 01881). Representative images of films grown on both glassy carbon and quartz are shown in Fig. 3.

Structural, elemental composition and morphology analysis.— Bulk elemental analysis of the deposited films was determined by inductively coupled plasma optical emission spectroscopy (ICP-OES) using a Perkin Elmer Optima 7300DV ICP-OES. After film growth, samples were prepared by punching out a Ø 0.953 cm coupon from a 0.051 mm thick polypropylene sheet and digesting under reflux in an aqua regia solution according to EPA method 6020A. The structure of the $Ir(C_5H_7O_2)_3$ and $Ru(C_5H_7O_2)_3$ precursor materials and the deposited films was probed by a Bruker D8 Advance X-ray diffractometer conFig.d with: a Ø 250 mm goniometer in Bragg-Brentano geometry; a Cu K_α (1.541 Å) source; and a compound silicon strip 1-dimensional LynxEye detector.

SEM images were captured using a FEI Quanta 250 FEG with a field emission source and imaged using a Everhart-Thornley SE (secondary electron) detector with an electron accelerating voltage of 20 kV and a sample height of 10 mm. X-ray energy dispersive spectroscopy (XEDS) was performed using an electron accelerating voltage of 10 kV and a working distance of 10 mm. The surface chemistry of the sample was examined on a PHI Multiprobe using a Mg K_α X-ray source. All binding energies were calibrated by placing the graphite C1s line at 284.6 eV. The XPS electron energy plot of the Ir and Ru peaks was fit by constraining the full-width at half-maximum (FWHM) of each photoelectric emission line to 2 eV; a value determined by the diameter of the analyzer, the pass energy and the spread of energies in the X-ray source. The fitting parameters were also set so that the ratio of the electron emissions between the doublet states of the core f level orbitals was set to 4:3. This ratio is derived from photoemissions having symmetries, defined by f orbitals, that define an angular momentum equal to three ($\ell = 3$) thus yielding a multiplicity ratio of $(2(\ell - \frac{1}{2}) + 1) : (2(\ell + \frac{1}{2}) + 1)$ which equals 4:3 (i.e., the ratio of the $f_{7/2}$ and $f_{5/2}$ doublet was fixed to 4:3).

Early-stage growth of the forming films (deposition time < 6 minutes) was examined to determine the particle shape, distribution, and

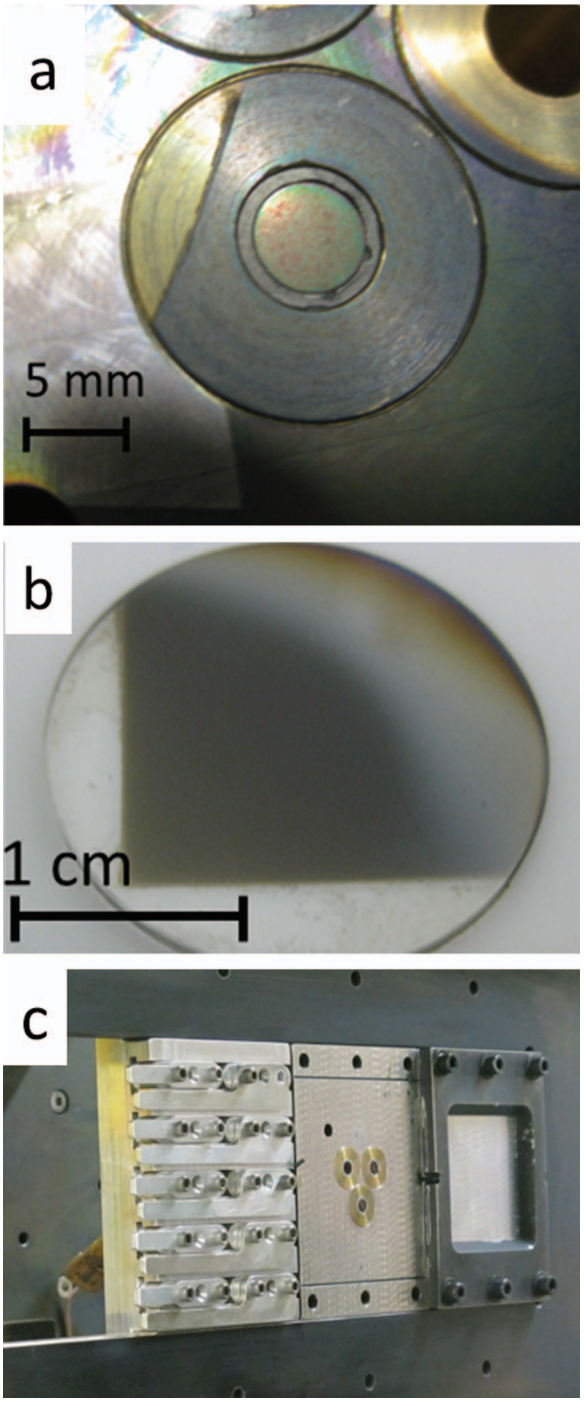

Figure 3. $Ir_xRu_{1-x}O_{2-y}$ deposited directly onto a) glassy carbon rotating disk electrode, b) quartz substrate, and c) TEM grid holder with glassy carbon and masked polypropylene substrate blocks.

size as they populated the TEM grid surface. A series of electron micrographs were collected with: a JEOL 2010 FasTEM (a field emission JEOL 2010 TEM operating at 200 kV), and an aberration-corrected Hitachi HD2700C S/TEM. The grids, placed at an equivalent stand-off distance to the electrodes, were removed at 90 and 240 seconds. Film formation from impinging nanoparticles is ideally suited to study using the TEM because, in the early stages of growth, the films are thin enough so as to be transparent to electrons. Additionally, the Cu grids do not require additional sample preparation.[82]

Electrochemical determination.— All electrochemical measurements were performed in a three-electrode, single-compartment half-cell using a reversible hydrogen electrode (RHE) (ET071 Hydroflex, eDAQ) as the reference electrode. A Pt wire (0.5 mm OD × 152 mm L, 99.95%) in a fritted tube was used as the counter electrode (AFCTR5, Pine Instruments). All potentials reported in this paper are relative to a RHE immersed in 0.5 M H_2SO_4 at 25°C. The sulfuric acid choice was based on approximating the conditions an electrode experiences when bonded to Nafion. Cyclic voltammetry was performed using a potentiostat, controlled with Nova software (Metrohm, PG-STAT101). Rotating disk voltammetry was performed using an ASR rotator (AFMSRCE, Pine Instruments). The whole 125 mL half-cell (AKCELL3, Pine Instruments) was surrounded by a water jacketed sheath with the water temperature thermostated to 25°C (Isotemp 3016D, Fisher).

Results and Discussion

Precursor decomposition.— The Ir and Ru acetylacetonate precursors decomposed completely, see Fig. 4, at 326°C and 316°C respectively, in the TGA. As a point of reference, non-premixed combustion of toluene and oxygen reaches temperatures above 1500°C; ample energy to decompose the precursor material exists in an oxy-toluene flame.[83]

The RSDT combustion system uses a pre-mixed jet-flame with pure oxygen. The benefits of this configuration over conventional air-fired combustion results in increased temperature, better thermal efficiency, reduced pollutant emissions, and improved flame stability.[84] However, industrially the costs associated with use of pure oxygen can be prohibitive. Recent advances in air-separation technology, rising fuel prices, stricter government emissions standards, and the need to reduce atmospheric carbon dioxide (CO_2) emissions may extend the window of economic viability for oxygen enhanced combustion.

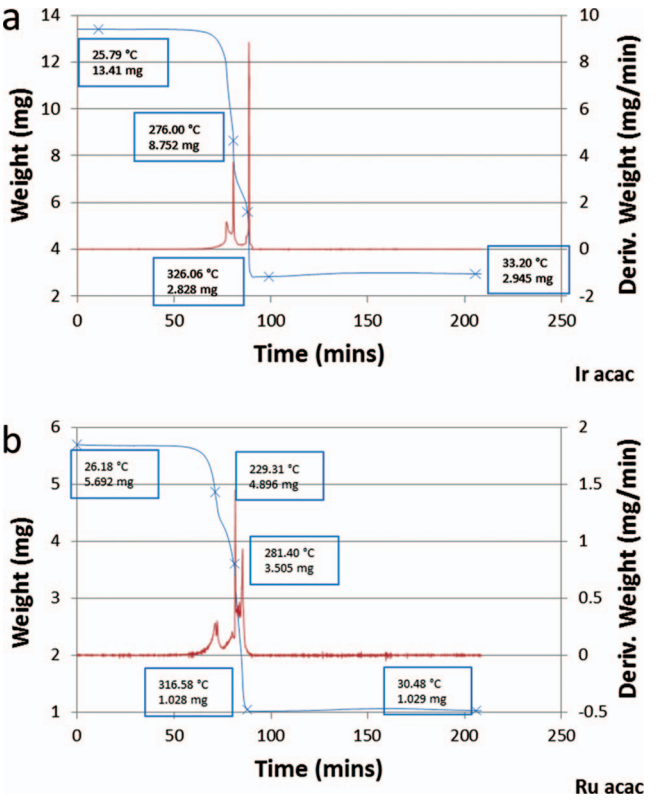

Figure 4. Decomposition profile for a) Ir (III)-acetylacetonate (13.41 mg) and b) Ru(III)-acetylacetonate (5.69 mg) heated in air at a rate of 5°C/min to 550°C.

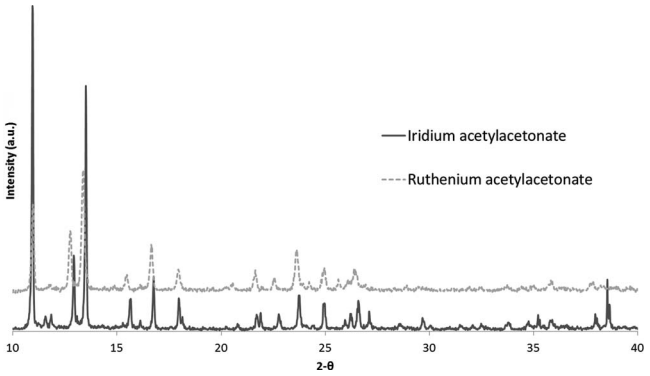

Figure 5. Indexed diffraction intensities for Ruthenium (III) 2,4 pentanedionate and Iridium(III) 2,4, pentanedionate, as used in this study.

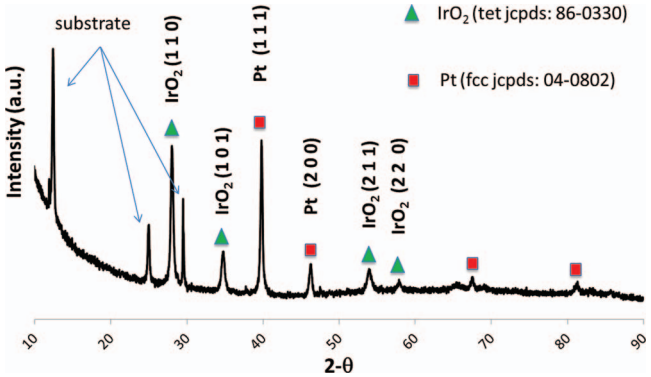

Figure 7. $Ir_xPt_{1-x}O_{2-y}$ bulk diffraction intensities after 4 hours heat-treatment at 800°C, Cu radiation (λ = 1.54 A).

X-ray diffraction (XRD).— The $C_{17}H_{24}O_4Ir$ was indexed to a monoclinic lattice space group P21/c (JCPDS 23–1711) with major peaks occurring due to the (0 0 2) and (1 0 2) planes at 8.23 Å and 6.68 Å respectively, shown in Fig. 5. Likewise the $C_{17}H_{24}O_4Ru$ precursor shows similar reflections at low 2θ (larger planar spacing). The desired RuO_2 and IrO_2 phases do not show any reflections below 28° 2θ; this serves as a good quality control check to ensure no bulk precursor is in the final film. For trace analysis of acetylacetonate moieties, in the deposited film, TD GC/MS (thermal desorption gas chromatography/mass spectroscopy) has proven useful in past studies.[85]

Ruthenium and iridium oxide both adopt a tetragonal lattice with space group P42/mnm and major reflections occurring due to the (1 1 0) planes at ∼28° 2θ and (1 0 1) planes ∼35° 2θ (JCPDS 43–1027 and 86–0330). Metallic Ir adopts a face centered cubic lattice (JCPDS 65–1686) having primary reflections at 40.76° 2θ (d = 2.211 Å) and 47.421° (d = 1.196 Å); these reflections correspond to the (1 1 1) and (2 0 0) planes. Metallic Ru forms a hexagonal lattice with space group P63/mmc (JCPDS 06–0663). Initially no diffraction was observed on the as-deposited films; presumably the diffraction was attenuated due to a combination of the film: thickness, porosity, and the nanocrystalline domain size of the oxides. The temperature of the coated quartz substrate was then ramped to 800°C in a tube furnace and held for 4 hours; the heating was employed to examine the resultant film properties. The post heating diffraction intensities, Fig. 6, indicate that the majority of the reflections are due to IrO_2, RuO_2, or a combination of $Ir_xRu_{1-x}O_{2-y}$. Ru metal is also present to a lesser extent having reflections at 44.007° 2θ (d = 2.056 Å) and 38.388° (d = 2.343 Å) corresponding to the (1 0 1) and (1 0 0) planes. Quantification of the ratios by diffraction was not possible due to a lack of suitable standards. No evidence of Ir metal or precursor is present in the diffraction pattern.

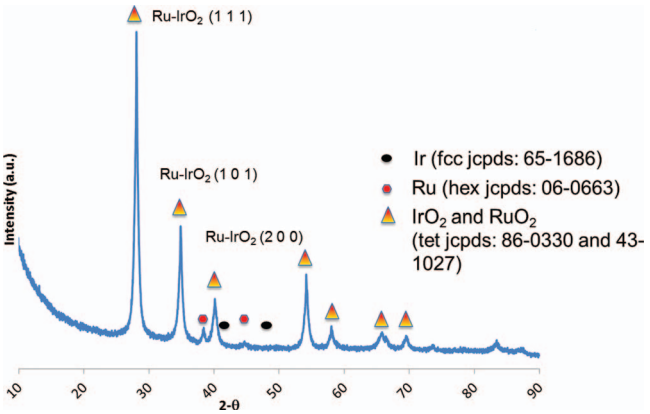

Figure 6. $Ir_xRu_{1-x}O_{2-y}$ bulk diffraction intensities after 4 hours heat-treatment at 800°C, Cu radiation (λ = 1.54 A).

The desired BOE $Ir_xPt_{1-x}O_{2-y}$ adopts a rutile type structure; metallic Ir and Pt should be absent. Examination of the diffraction intensities, Fig. 7, indicates that two distinct phases, indexed to the tetragonal IrO_2 (JCPDS 86–0330) and face centered cubic platinum metal (JCPDS 04–0802), are present. This indicates that a sizeable portion of the platinum was not incorporated into the crystal structure of the desired $Ir_xPt_{1-x}O_{2-y}$. Studies with various ratios of platinum in the rutile lattice of the IrO_2 show a phase transformation to cubic around Ir:Pt 50/50 mole ratio; a corresponding unit cell volume increase occurs with expansion along the c-axis from 3.160 to 4.137 Å.[86]

The boiling point (b.p.) and melting point (m.p.), of each metallic species, suggests a reason for the reduced incorporation of Pt into the IrO_2 lattice. Pt has a m.p. of 1769°C and a b.p. of 3827°C. Among the transition metals these physical properties are high; however, they are significantly lower than Ir (m.p. 2447°C, b.p. 4427°C) or Ru (m.p. 2337°C, b.p. 4152°C). Crystallization of the Pt vapors occurs prior to the crystallization-oxidation sequence in the forming IrO_2. Pt oxidation is negligible, hence the lack of PtO or PtO_2 in the diffraction pattern. The Pt continues to progress through the stages of particle formation: monomer, cluster, primary, and finally nanoparticle at a faster rate than the forming IrO_2. This does not preclude incorporation of some of the Pt into the IrO_2 lattice but as the reaction proceeds down the length of the flame the concentration of available Pt is diminished. A similar argument explains the presence of minor amounts of Ru metal in the $Ir_xRu_{1-x}O_{2-y}$ film; however, in this case the differences in m.p. and b.p are smaller (i.e., 110°C and 275°C respectively).

Surface analysis and elemental composition.— Bulk elemental analysis by ICP-OES suggests an Ir to Ru ratio of 59:41. This ratio is close to the 50:50 nominal value calculated from the mixed precursors. The same elemental analysis for Ir to Pt was 56:44. A typical SEM micrograph of the as-deposited $Ir_xRu_{1-x}O_{2-y}$ film (no thermal treatment) is depicted in Fig. 8a, along with the corresponding XEDS plot. The micrograph shows that nucleation and growth of the film appears to have occurred uniformly across the quartz plate except for a few regions of faintly visible clustered growth. These island-growth regions have dimensions of several hundred nanometers. An area of the film, free of the clusters, is shown in Fig. 8b. Film formation is much more uniform in coverage and exhibits an interconnected and interdigitated growth. Areas of clustered growth are noticeably absent in this region. The film has noticeably open pores which contribute to an open and non-tortuous pathway in the out-of-plane direction. The in-plane open pores, around the growth centers, follow a tortuous path. The XEDS plot shows the expected Ir characteristic X-ray Lα and Mα emission lines; 9.174 and 1.978 keV respectively. The corresponding Lα line for Ru is prominent at 2.558 keV. The large peak at 1.74 keV is due to the quartz substrate on which the film was grown.

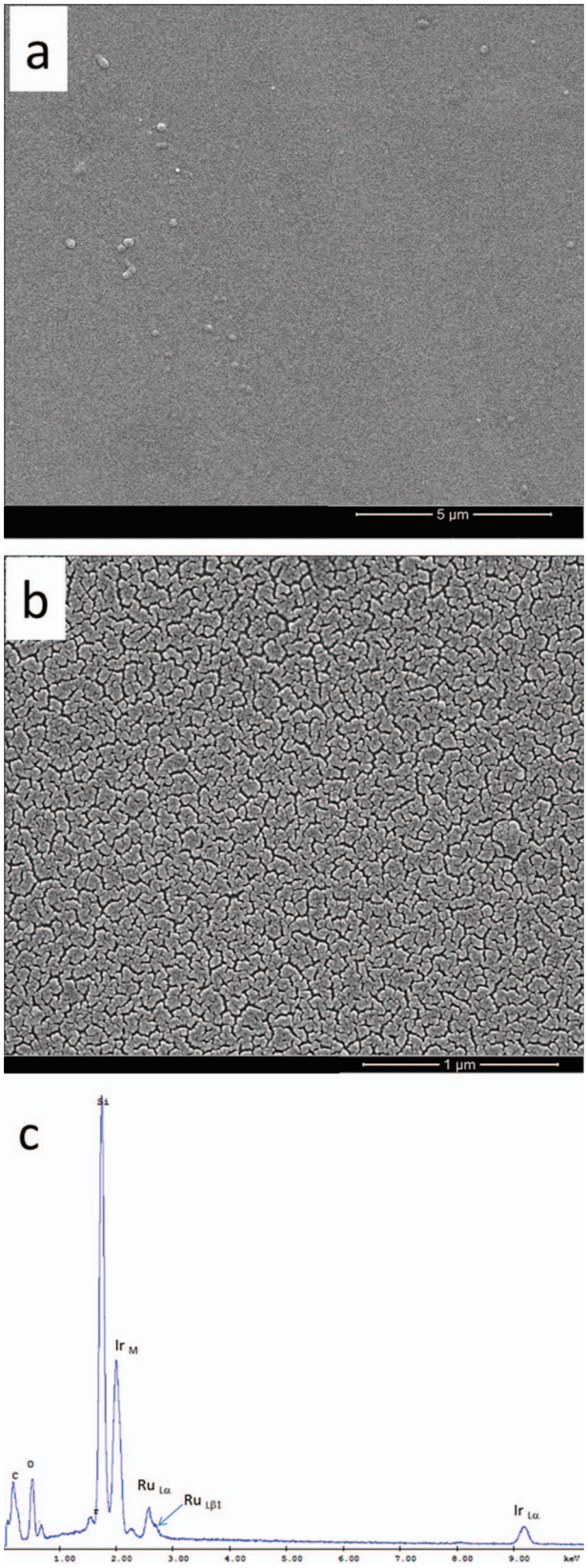

Figure 8. a,b) SEM micrographs of $Ir_xRu_{1-x}O_{2-y}$ film with c) corresponding XEDS plot.

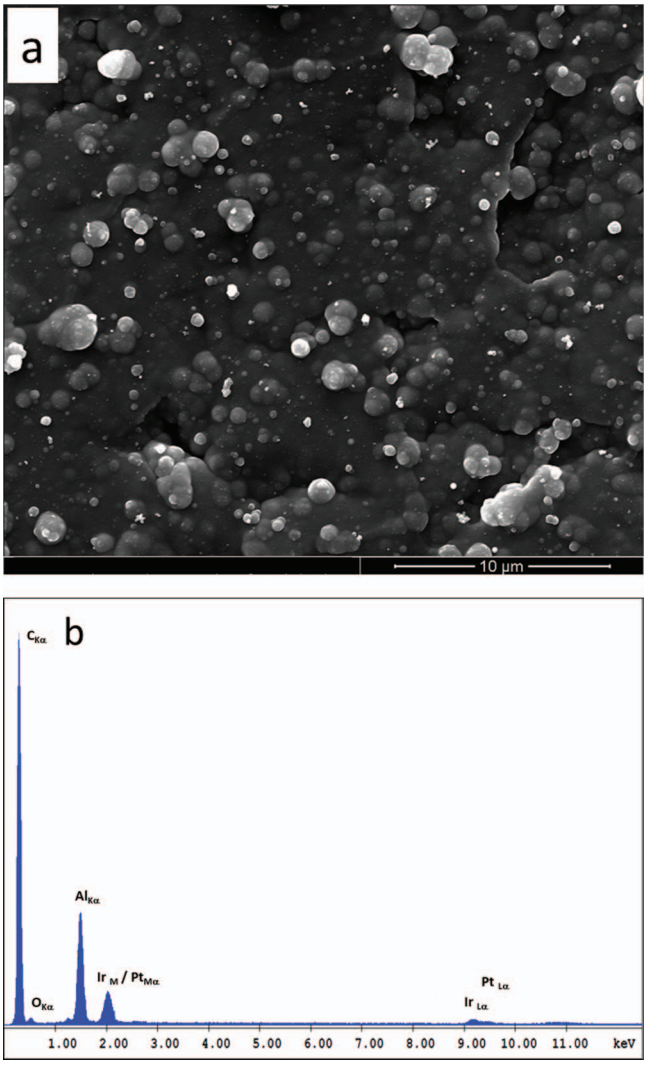

Figure 9. a) SEM micrograph of $Ir_xPt_{1-x}O_{2-y}$ film deposited on an Al stub and b) corresponding XEDS plot, 30 kV electron beam accelerating voltage.

A typical SEM micrograph of the as-deposited $Ir_xPt_{1-x}O_{2-y}$ film (no thermal treatment) is depicted in Fig. 9a, along with the corresponding XEDS plot. The micrograph, in comparison to the $Ir_xRu_{1-x}O_{2-y}$ film, exhibits a marked increase in the number of clustered growth centers and these clusters range in diameter from several hundred nanometers to several microns. Other prominent features of the micrograph are; steps and crevices spanning several microns; more areas that charge from exposure to the electron beam; and growth centers that are in various stages of coalescence. A major difference between the two films is the composition and morphology of the underlying substrate. The $Ir_xRu_{1-x}O_{2-y}$ was grown on a smooth quartz disk while the $Ir_xPt_{1-x}O_{2-y}$ film was grown on an Al SEM pin stub specimen mount. Electron imaging of the aluminum specimen mount (not shown) reveals scratches, ledges and crevices formed during fabrication; the specimen mount has a significant amount of surface morphology. The initial stages of film growth (e.g., adatom diffusion, island formation, and specific island morphology) are undoubtedly influenced by the underlying microstructure of the substrate leading to a difference in the developing morphology.[87,88] An alternative explanation is that the in-flight particle formation, of the $Ir_xPt_{1-x}O_{2-y}$, proceeded at a faster rate; the accelerated growth ultimately leads to larger particles that impact and stick to the substrate. These larger particles then act as growth centers that express themselves with column or dome shaped features on the micron scale. The XEDS plot shows the expected

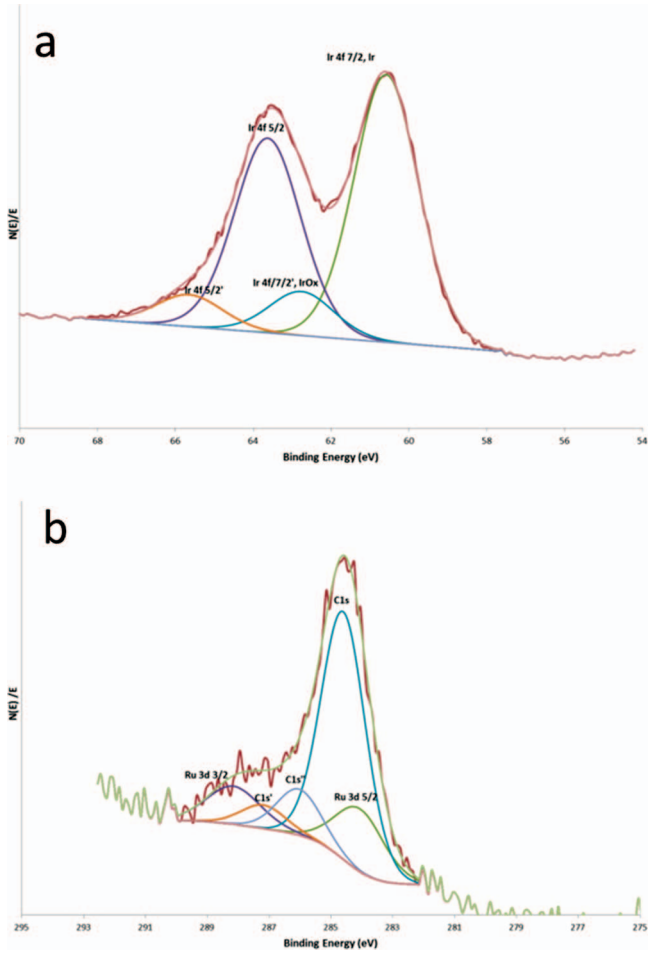

Figure 10. XPS electron energy spectrum of a) Ir 4f and a) Ru 3d electrons as measured from the $Ir_xRu_{1-x}O_{2-y}$ film deposited on a polypropylene substrate.

characteristic Ir L_α emission at 9.174 eV. However, discriminating between the charactersitic Pt Mα (i.e., 2.048 eV) and Ir Mα (i.e., 1.978 eV) emission energies was not possible. The Pt L_α characteristic emission at 9.441 eV is very faint.

Segregation of Ir, at the film surface, has been reported in the literature using XPS studies;[31] the segregation was attributed to expansion, of the slightly larger Ir^{4+} ion, which was better accommodated at the surface compared with the bulk. Evidence for segregation is suggested by the observation that the maximum deviation of the Ir/Ru ratio from bulk composition, by XPS analysis, falls in the same range as the maximum deviation from Vegard's law. Although Hutchings et al. suggest that this is just as likely due to ruthenium possessing a higher oxidation potential leading to enrichment during crystal growth and consequently a surface deficiency. Kodintsev and Trassatti found a homogeneous depth distribution when the electrodes were prepared by multi-layer thermal decomposition of the prerequisite chlorides; the authors note that there was compositional variation in the near-surface layer and concede that it is difficult to rest on a reference standard since the sensitivity factors depend on oxygen content.[89] The oxygen content is known to vary sharply near the surface.

XPS reveals, see Fig. 10a and Table I, that the Ir $4f_{7/2}$ and $4f_{5/2}$ photoemission doublet, arising from the $Ir_xRu_{1-x}O_{2-y}$ film, is separated by 2.92 eV. Reference values for the Ir $4f_{7/2}$ to Ir $4f_{5/2}$ binding energies are 60.6 eV and 63.55 eV; the doublet has spin-orbital separation energy of 2.95 eV.[90] The shape of the Ir 4f doublet photoelectron doublet emission suggests the existence of both Ir^0 and Ir^{4+}; the surface concentration appears enriched in metallic Ir since the oxide only accounts for 15% of the photoemission intensity. It is known that Ir metal forms

Table I. XPS data for deconvoluted Ir 4f peaks.

Name	B.E. (eV)	FWHM	Area	% Area
Ir $4f_{7/2}$ Ir	60.58	1.958	1880.16	49.07
Ir $4f_{5/2}$	63.63	2.019	1410.12	36.8
Ir $4f_{7/2}$' IrO_2	62.76	1.958	309.34	8.07
Ir $4f_{5/2}$'	65.64	2.019	232.01	6.06

Table II. XPS data for deconvoluted Ru 3d and Cs peaks.

Name	B.E. (eV)	FWHM	Area	% Area
Ru $3d_{5/2}$	283.7	1.851	122.06	15.96
Ru $3d_{3/2}$	288.16	2.044	81.42	10.64
C1s	284.6	1.689	438.01	57.25
C1s′	287.19	1.689	41.81	5.46
C1s″	286.04	1.689	81.74	10.68

a multilayer oxide; this layer arises during potentiodynamic cycling between water adsorption and onset of O_2 evolution (i.e., start-stop conditions in electrolysis) and results in a progressive oxidation of an Ir film.[91,92] This film was not subjected to cycling and was analyzed as prepared. The presence of Ir^0 at the surface is not congruent with the findings from the XRD data; the apparent contradiction can be explained by the length scale of the sampling technique. XRD probes the bulk sample whereas XPS is a very surface sensitive technique that is only sensitive to the top few surface layers.

Unfortunately, the Ru 3d doublet photoemissions are in coincidence with carbonaceous residues on the sample (i.e., the C1s photoemission); this overlap obscures analysis as shown in Fig. 10b and Table II. Photoemissions arising from the elemental Ru $3d_{5/2}$ and $3d_{3/2}$ doublet have binding energies of 280.0 eV and 284.1 eV respectively; this gives rise to a peak energy separation of 4.1 eV.[90] The absence of peaks in this region, Fig. 10b, suggests a relatively large shifting of the Ru to higher binding energies. The reference RuO_2 binding energy of the $3d_{5/2}$ peak is 283.2 eV which is very close to the observed 283.7 eV peak in our sample. The corresponding $3d_{3/2}$ peak is located at 288.16 eV corresponding to a spin-orbital splitting distance of 4.46 eV close to the literature expected value of 4.1 eV. These results suggest that Ru exists primarily in the oxidized Ru^{4+} state. Concerning the aforementioned distinction between Ir segregation mechanisms (i.e.; strain relief versus enrichment during crystallization) it should be noted that synthesis in this study was done rapidly and from a dry state which would minimize or eliminate diffusional effects that have longer time constants and favor a mechanism in which one component selectively crystalizes first. The Ir metal peaks are an order of magnitude higher than the RuO_2 peaks and 6 times larger than the corresponding oxide suggesting a surface enriched in Ir metal.

The X-ray diffraction results for the $Ir_xRu_{1-x}O_{2-y}$ film are in contrast to the XPS surface analysis which suggests the as-deposited sample is rich in Ir metal and lacks Ru metal. The apparent discrepancy is due to the heat-treatment step which may have oxidized any residual Ir metal. It is not clear why Ru metal is present in X-ray diffraction after heat-treatment while the XPS shows none on the surface. This would imply a segregation of the oxidized species to the surface. Further work is needed to examine the cause of this discrepancy as well as using thin-film XRD techniques to identify the structure of the as-deposited film and perhaps examine the evolution of structure before and after polarization scans.

Transmission electron microscopy.— Evidence for the presence of a core-shell particle enriched in RuO_2 could be elucidated by a z-contrast aberration corrected (on probe) STEM of the film as it forms on the collection grid (shown in Fig. 11).

Image contrast in Fig. 11 arises from differences in the atomic number between the Ir (z = 77) and Ru (z = 44) in the addition to the number of atoms vertically aligned with the electron beam. Fig. 11

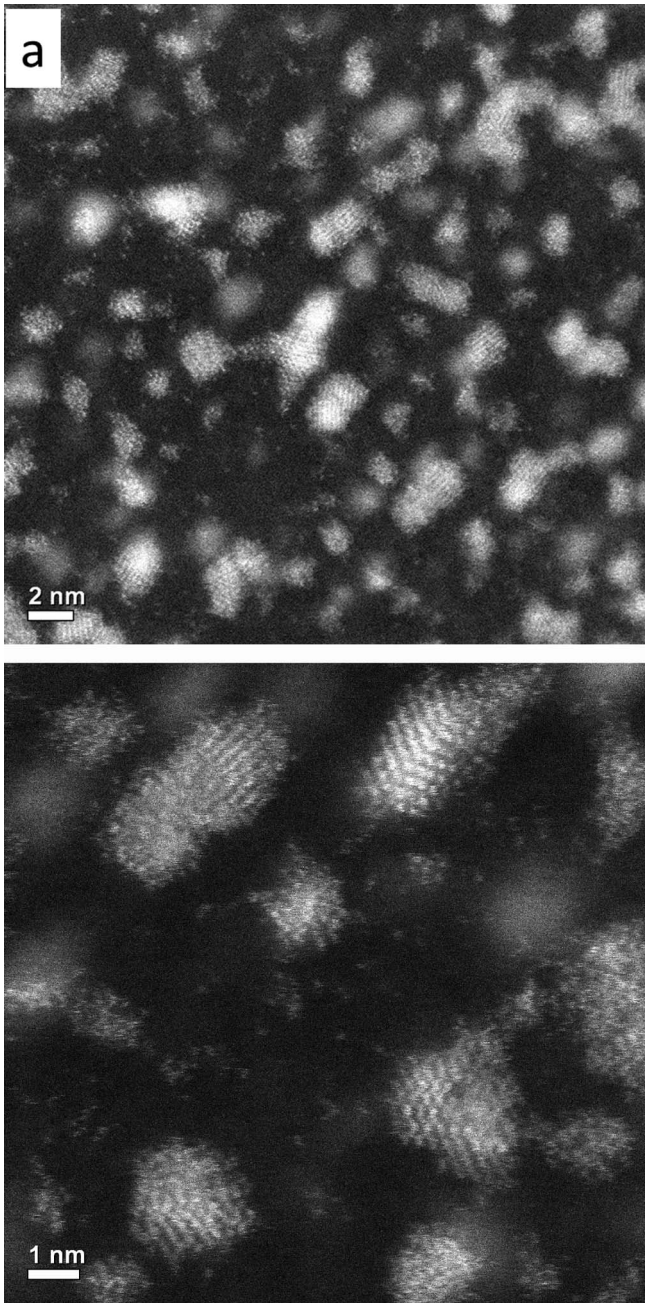

Figure 11. HAADF image from a Hitachi HD2700C STEM of $Ru_xIr_{1-x}O_{2-y}$ particles (grid exposed to deposition for 90 s.

shows that most of the representative particles are 1-2 nm in length and have aspect ratios close to 1 while the larger clusters exhibit aspect ratios of 2–3. It should be noted that the larger clusters result from the coalescence of two or more particles; a grain boundary is shared between the particles. The existence of two distinct types of particles: coalesced and single grain, suggest that two film formation mechanisms occur simultaneously. This observation also suggests that particles are arriving at different stages of formation. If homogeneous nucleation occurred sometime during the flight of the particle then, as the deposition time progressed, a growing film surface would have a uniform distribution of particles. Advanced stages of film growth would resemble extensions of the earlier stages; except that the number frequency of particles would be higher (i.e., a film grown for a longer time would exhibit the same particle size and distribution but have a denser coverage). This deposition route can be considered a ballistic type mechanism since the particles, already fully formed, hit the substrate and stick. The efficiency of this mass transfer is measured by the sticking coefficient.

However, heterogeneous deposition from the vapor phase can be considered if the film growth preferentially occurs on nucleated particles attached to the substrate. In this mechanism the incoming metal vapors are attracted to energetically favorable sites on exposed facets of the growing film. Particles larger than the primary particle length appear to exhibit twin boundaries (white arrow in Fig. 11b) and grain coalescence. Particles coated both sides of the lacey carbon grid and this was observed by changing the focus plane. These findings are congruent with a process of nucleation and growth at the surface of the substrate that lead to conformal, not line-of-sight, coatings; this suggests a mechanism whereby at least some crystallization occurs directly from the vapor phase onto the substrate. Fig. 11 also shows a number of clusters having size ranges between one to several angstroms. These clusters have not formed into fully crystallized particles indicated by a periodic longer range order.

Cu grids exposed to the deposition process for 90 s and 240 s were also examined in TEM transmission mode using a JEOL 2010 FasTEM; contrast is this mode is due to diffraction. Fig. 12 shows that the difference in contrast is immediately evident due, in part, to the interference of the backing carbon film on the grid.

Compared to the image contrast in STEM mode, only the larger particles are clearly visible in these images. Of particular interest

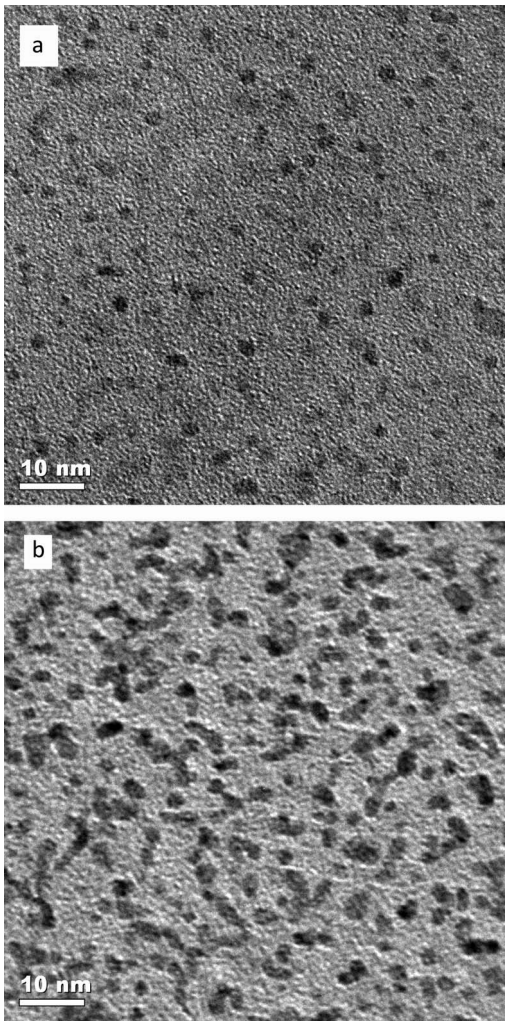

Figure 12. TEM image using a JEOL 2010 FasTEM of $Ir_xRu_{1-x}O_{2-y}$ particles using a grid exposed to the deposition for 90 s (a) and 240 s (b).

is the difference in coating coverage between the grids exposed for 90 s versus 240 s. The grid exposed to the deposition for 90 seconds reveals spherical islands of growth isolated from each other; the film growth at 240 s suggest that the incoming particles concentrate at the pre-existing islands. At 240 s the growth appears concentrated at points of previous deposition. This can be explained by a mechanism whereby favorable nucleation sites for the incoming vapors are provided by the previous growth centers or that the incoming fully formed ballistic particles have an increased sticking coefficient around these points. The average particle size slightly increases with collection time starting at ∼1.5–1.7 nm at 30 seconds (image not shown) and then leveling out to 2.2–2.3 nm for both 90 and 240 seconds. The distributions are mostly Gaussian in nature with some skewing of the distribution to larger sizes after 30 seconds. This skewing could be in part due to the difficulty in discerning the coalesced particles from individual particles. If the deposition mechanism was solely due to a vapor sublimation mechanism, on energetically favorable sites, then the individual crystal size of the growing $Ir_xRu_{1-x}O_{2-y}$ should increase with time. The observation that the crystal size levels out after 90 s would seem to rule out vapor sublimation as a major mechanism. Of note is that occasional larger particles (>15 nm) are observed although their frequency of observation is low. Since the substrate surface temperature is at or below 120°C during the entire deposition there is a large energetic barrier to surface diffusion and the deposited material is largely immobile once striking the surface.

Features similar to observations in the $Ir_xRu_{1-x}O_{2-y}$ system are repeated in $Ir_xPt_{1-x}O_{2-y}$, see Fig. 13. These images, of the growing film, were taken on a JEOL 2010 FasTEM in TEM mode using Cu grids exposed to the deposition for 90 s (top) and 360 s (bottom).

The 90s exposure in Fig. 13a highlights the branched structures formed during film growth; the branches form open pores in the

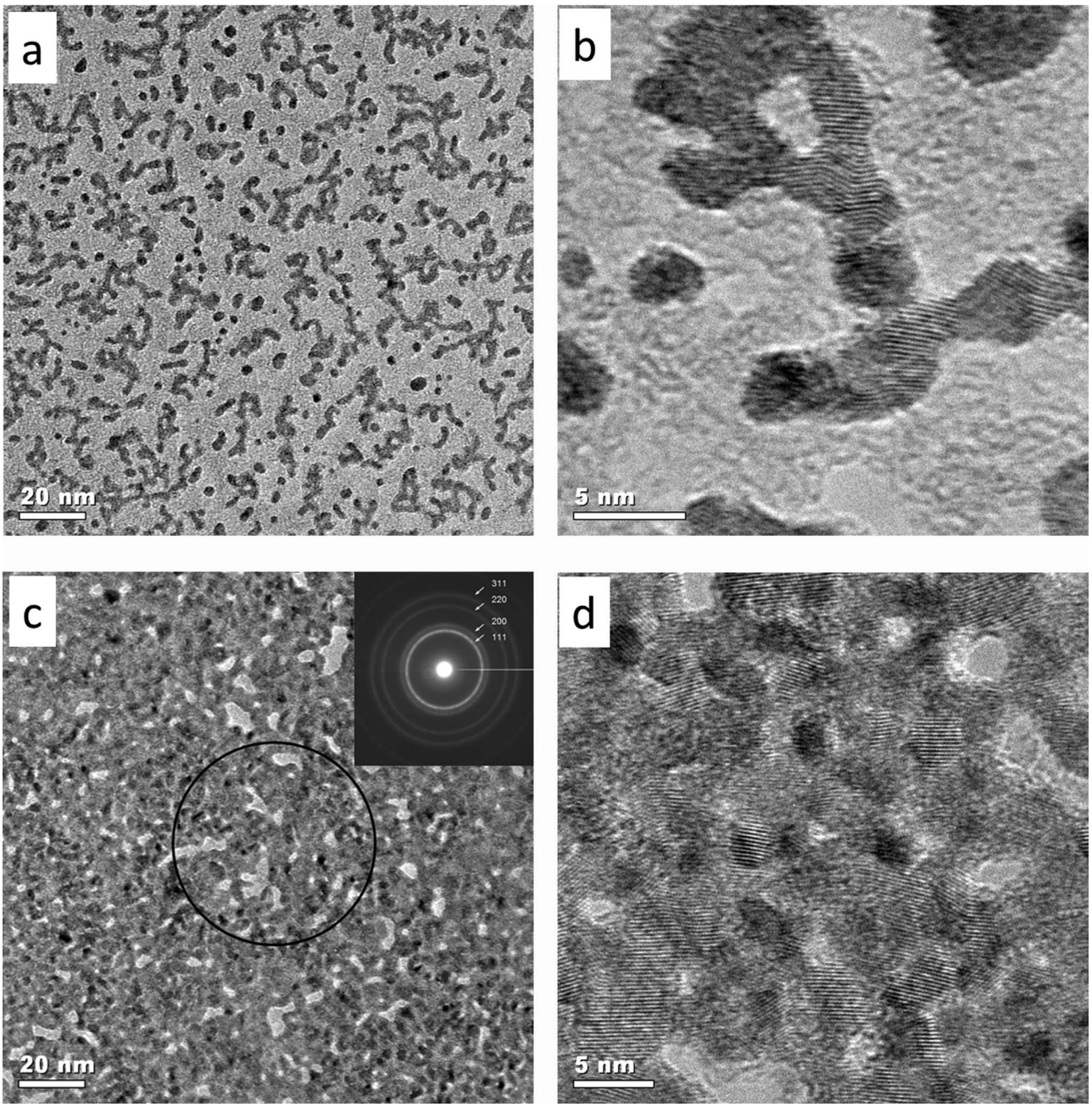

Figure 13. TEM image using a JEOL 2010 FasTEM of $Ir_xPt_{1-x}O_{2-y}$ particles using a grid exposed to the deposition for a,b) 90 s and c,d) 360 s.

forming film. There are also a few areas having un-branched spherical particles, less than 5 nm in size, with darker contrast. The irregular branched structures and the number of primary particles they contain compared to the agglomerate size are frequently described by the use of fractal theory.[61] Agglomerated powders have very different transport properties (diffusion, settling, etc.) compared to spherical primary particles and fractal theory is useful as a descriptor in determining the extent of agglomeration.[80] Fig. 13b highlights the boundaries formed by interparticle coalescence (the fusing of two or more particles). Interparticle bond energies can exist as a spectrum from weak van der Waals forces (soft agglomerates or just agglomerates) to stronger solid state necks (hard agglomerates or aggregates).[93] The onset of agglomeration occurs when the characteristic time for coalescence (i.e., sintering) (τ_s) exceeds the characteristic time for particle collisions (τ_c). When τ_s increases much faster than τ_c ($d\tau_s/dt \gg d\tau_c/dt$ after $\tau_c = \tau_s$) soft agglomerates of spherical particles are formed, while oblong particles (hard agglomerates) are formed when τ_s increases slightly faster than τ_c ($d\tau_s/dt > d\tau_c/dt$).[80,94] Fig. 13b shows definite necks between the primary particles with a range of crystallite orientations as well as crystal twinning. Alongside the agglomerates are individual particles having no extent of agglomeration suggesting again that coalescence in the flame zone does not occur for all particles. At 360 seconds most of the space between the particles is not visible, due to layer-by-layer stacking of incoming branched agglomerates, there are however a few uncovered regions; this testifies to the porous nature of the forming film using these processing conditions. The selected area electron diffraction (SAED) in Fig. 13, highlighted by circle, shows the strong diffraction bands of metallic platinum metal and attests to the crystallinity of the forming film. A more detailed observation of Fig. 13d reveals that most of the grid is coated although some uncoated regions still exist. The built up particle deposits reveal a range of exposed crystallographic orientations as well as differences in contrast that suggest thicknesses variations leading to a nanoporous textured film.

Fig. 14 is an image of a branched $Ir_xPt_{1-x}O_{2-y}$ particle taken on a JEOL 2100 HRTEM. This image shows, in better detail, the interface between the individually formed crystals that have begun to sinter together in random orientations. In addition to the highly branched structure there is also a particle with only a small neck connected to another particle indicating that these particles experienced significantly less sintering during time-of-flight.

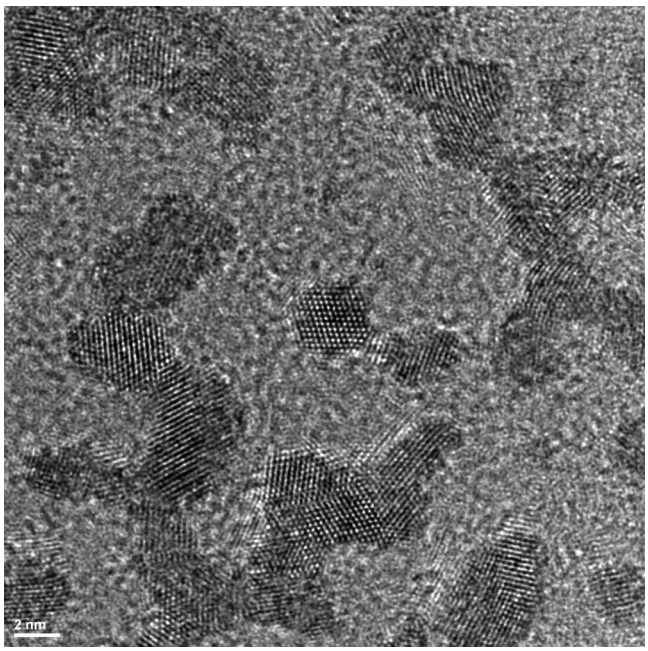

Figure 14. TEM image of $Ir_xPt_{1-x}O_{2-y}$ using a field emission JEOL 2100 TEM operating at 200 kV.

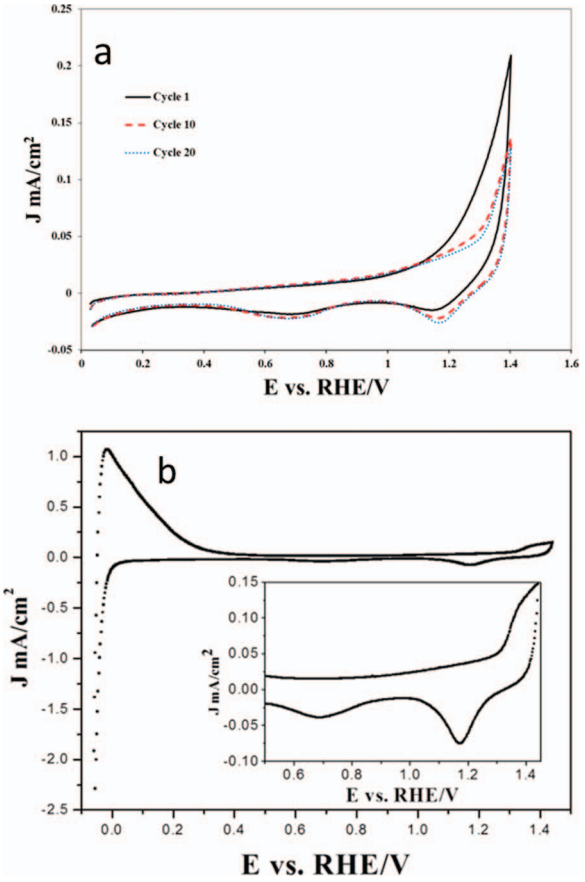

Figure 15. Cyclic voltammetry, scan rate 20 mV/sec, on $Ir_xPt_{1-x}O_{2-y}$ which shows the evolution of the current response with cycle number in the window of 0.05–1.4 V (a) and (b) once stabilized, the current response extending the lower potential to −0.05 V.

Cyclic voltammetry.— Cyclic voltammetry (CV), of the $Ir_xPt_{1-x}O_{2-y}$ film on Au, was utilized to better understand the water oxidation and oxygen reduction capacity of the BOE, the scans are shown in Fig. 15.

The CV response suggests the presence of a mixed IrPt oxide: H_2 absorption and evolution; O_2 reduction and evolution; and redox peaks for the IrO_2 Ir^{3+}/Ir^{4+} couple. The lowest potential was limited to 0.05 V during break-in of the electrode (Fig. 15a) and then reduced to −0.05 V (Fig. 15b). Once stabilized, the electrode's onset potential for H^+ adsorption occurred at 0.25 V; the cathodic current rose logarithmically until potential reversal at 0.05 V. The peak oxidation current resulting, from release of the adsorbed protons, occurs at −0.15 V and then decays over a broad range of potentials to ∼0.4 V. The onset potential for O_2 evolution is 1.32 V (see Fig. 15, inset). On the reductive side the Ir^{4+} to Ir^{3+} transition is evidenced by a broad peak at 1.18 V and the oxygen reduction on platinum occurs at 0.7 V.

In order to examine the suitability of the film toward oxygen evolution, the sample was cycled between 1.2–1.7 V, using a rotational speed of 900 rpm. The rotation prevents the gaseous O_2 product from blocking active sites during formation and continuously flushes the electrode with reactant. The results are plotted in Fig. 16. The sample was cycled 10 times and attenuation was observed with each cycle; this indicates degradation in the film or deactivation of the catalyst. The onset potential for oxygen occurred at 1.45 V on the first pass but then increases to 1.5 V by cycle 10. Visual inspection of the electrode after cycling showed that delamination of the film, from the gold

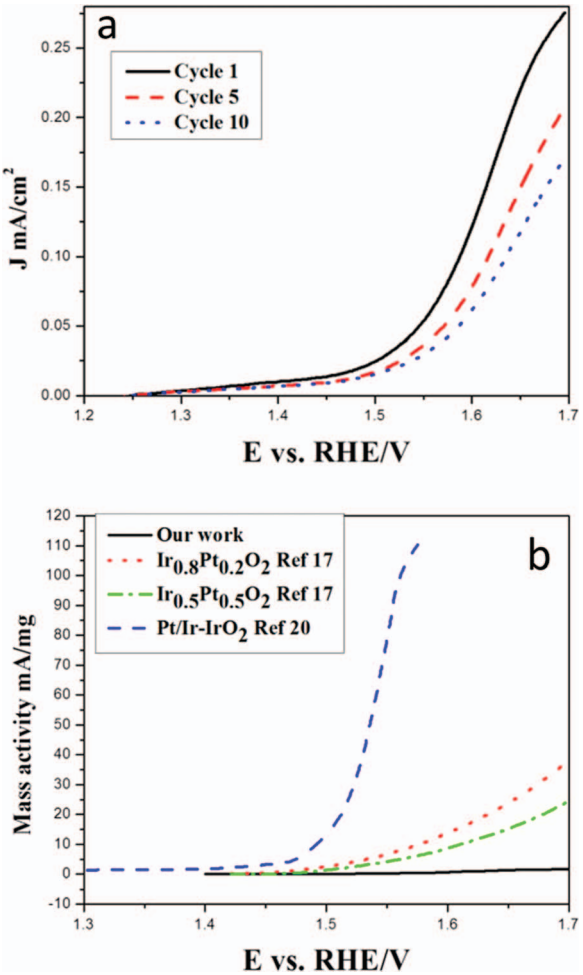

Figure 16. Linear sweep voltammetry of a $Ir_xPt_{1-x}O_{2-y}$ film in 0.5 M H_2SO_4 with a rotation speed of 900 rpm showing (a) the degradation with cycling and (b) comparison to literature values.

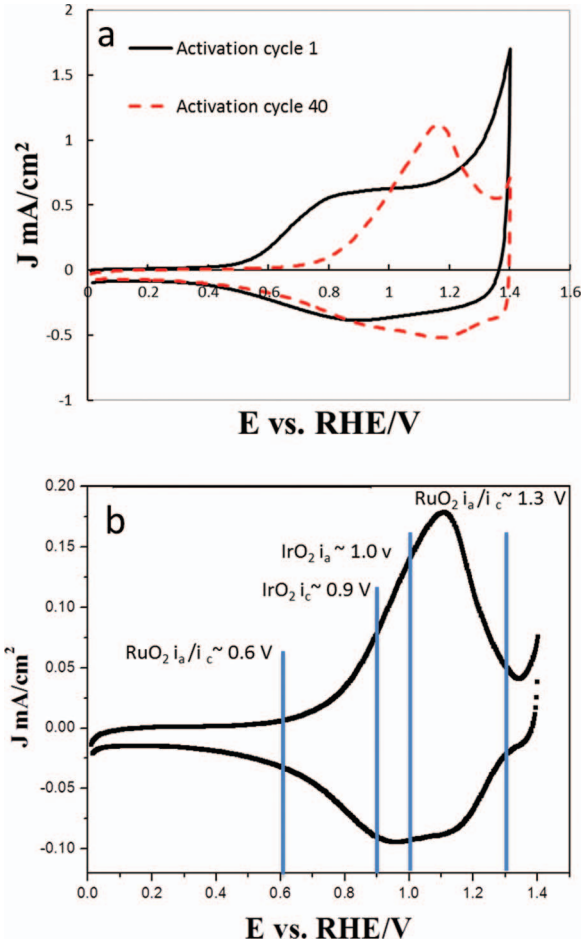

Figure 17. a) Cyclic voltammetry, scan rate 100 mV/sec, on $Ir_xRu_{1-x}O_{2-y}$ which shows the current response before repeated cycling (black) and after (red). The lack of sharp peaks suggests a variety of Ir and Ru active sites between 0.8–1.4 V and b) once stabilized the current response at a scan rate of 20 mV/sec. The expected redox potentials from literature for the respective metal oxides are marked for reference.

substrate, had occurred. A closer inspection of the film by SEM revealed pitting spots. A comparison of the O_2 evolution current, normalized to the metal oxide loading, with literature values[86] is shown in Fig. 17. The poor performance of the film highlights the need to better understand adhesion of $Ir_xPt_{1-x}O_{2-y}$ in bifunctional acidic environments. The spallation of films prepared by RSDT has not been observed in past studies using Pt[37] or in this study with $Ir_xRu_{1-x}O_{2-y}$. The obvious testing differences are that neither of these last two systems, the Pt or the $Ir_xRu_{1-x}O_{2-y}$, showed both appreciable H_2 and O_2 generation current. To confirm the delamination, a second film was deposited under the same conditions; the entire film came off as one piece into the electrolyte as before. Pt is known to be unstable in acid at high potentials; in light of the diffraction data (Fig. 7) showing separate phases of Pt and IrO_2, the delamination can be explained by Pt dissolution.[95]

CVs of the $Ir_xRu_{1-x}O_{2-y}$ deposited electrode were examined first on glassy carbon and then on Au disks; due to corrosion of the underlying glassy carbon the upper potential was limited and all O_2 evolution experiments were done using Au as the substrate. The water window (i.e., between the potentials of H_2 and O_2 evolution) of the film was examined by first cycling at 100 mV/s and then at 20 mV/s between 0–1.4 V. The cycling was done without rotation in N_2 purged 0.5 M H_2SO_4 electrolyte; the results are shown in Fig. 9. One of the interesting features of Ir metal is its tendency to form irreversible thick oxide layers (i.e., a hydrated film), during potentiodynamic cycling, within the water window (4, 24-25). The main anodic peak, corresponding to the IrO_2 III/IV couple, occurs at 1 V while the cathodic peak is centered at 0.9 V. RuO_2 is known to have a more symmetrical redox couple occurring at 0.6 V and a larger peak-pair at 1.3 V.[43] Fig. 17 shows that after 40 cycles, using a 100 mV/s rate, a very pronounced anodic peak appears at 1.15 V and a corresponding cathodic peak is observed at ~1.2 V; both of these peaks are attributed to the RuO_2 redox couple. The cathodic peak is somewhat obscured by a much broader background current.

It is seen in Fig. 17 that the H^+ adsorption peaks are missing since oxides do not easily promote H^+ adherence on surface. Activation of the film is noted during cycling (Fig. 17a) although there is no expanding current. The expanding current refers to changes in the CV, resembling a capacitive response, attributed to an increase in the number of accessible charging sites; the effect is caused during the hydration process of "fresh" IrO_2 films.[39] Broad undefined peaks, in the cathodic region of Fig. 17b, indicate a variety of Ir-Ru active sites with a range of formal potentials. Cyclic voltammetry of the as-deposited films show that the expected redox potential waves for pure IrO_2 are not well resolved. The RuO_2 peak was also not observed at lower potentials but was prominent for charge transfer at 1.3 V.

Fig. 18 illustrates that $Ir_xRu_{1-x}O_{2-y}$ films have a 1.5 V wide "water window" of stability; this is because evolution of H_2 on oxide surfaces will occur only at very negative potentials relative to Pt. In Fig. 18 the onset current from H_2 evolution does not occur until 0 V and even at −0.05 V the H_2 evolution current is small. The onset current for O_2 evolution occurs at 1.4 V. Fig. 18b shows that at 1.6 V there is

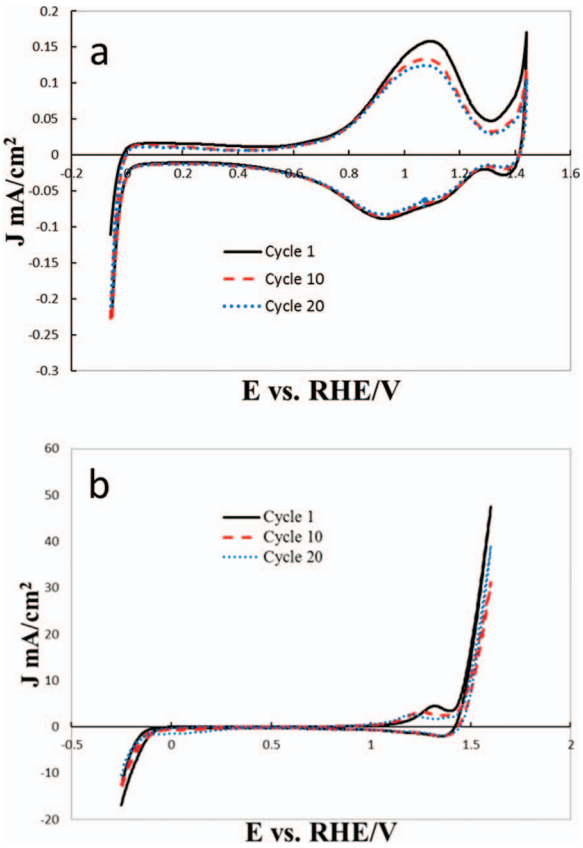

Figure 18. Cyclic voltammetry of $Ir_xRu_{1-x}O_{2-y}$ a) limiting the upper peak vertex voltage to within the "water window", and b) extending the upper peak vertex voltage to to 1.6 V.

significant current being generated by the electrode. In these experiments there was concern over the integrity of the glassy carbon electrode and background corrosion currents.

In order to extend the voltage range to the higher potentials required for appreciable O_2 evolution and to minimize the background corrosion currents from the support disk; a mirror polished Au electrode was used as the substrate. Fig. 19 shows the current response from the as-deposited film; reference markers indicate the known RuO_2 and IrO_2 redox potentials. There is initially a broad anodic peak centered at 1.1 V that shifts to 1.3 V and becomes more distinct after only a few cycles.

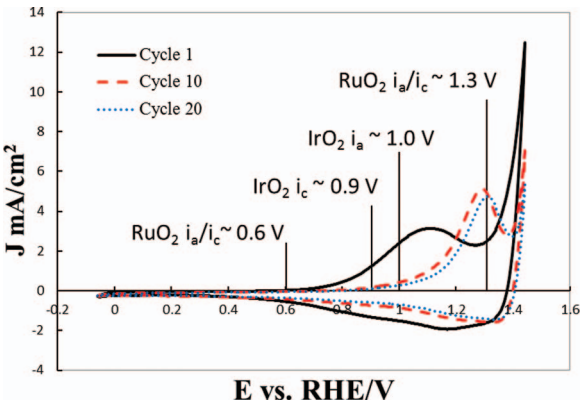

Figure 19. Plot showing the voltage current response in $Ir_xRu_{1-x}O_{2-y}$ films, deposited directly onto a Au substrate. The literature referenced redox potentials for Ir and Ru oxides are indicated by vertical lines.

The cathodic peak observed ~1.17 V flattens out and becomes less clear with a barely discernible peak shift of + 0.05 V. A clear shift in the onset potential, for O_2 evolution, increases from 1.3 V to 1.4 V within 10 cycles. The redox potential waves for pure IrO_2 are not well resolved. The expected RuO_2 redox peak at 0.6 V was not observed, however, a prominent charge transfer peak exists at 1.3 V. Once again the broad and not very well defined peaks indicate a variety of Ir-Ru active sites with different formal potentials.

Oxygen evolution using linear sweep voltammetry.— In order to evaluate the suitability of the thin film, deposited by RSDT, as a candidate for O_2 evolution; a series of polarizations between 1.2 and 2.0 V were initiated. The electrolyte composition (i.e, N_2 purged 0.5 M H_2SO_4) was kept the same as in the CV scans. An electrode rotation rate of 900 rpm and 1600 rpm was used to remove the oxygen evolved at the surface and to prevent the ensuing ohmic drop during polarization. However, above ~1.7 V scatter from the gas bubbles forming on the electrode becomes prominent regardless of the rotation rate.

Fig. 20a shows that the oxygen evolution onset begins around 1.45 V and appears to shift slightly higher potentials ~0.05 V within 5 cycles, at a rotation rate of 900 rpm. At 1600 rpm the onset shifts to 1.5 V. There is a 30% decrease in current after 10 cycles when

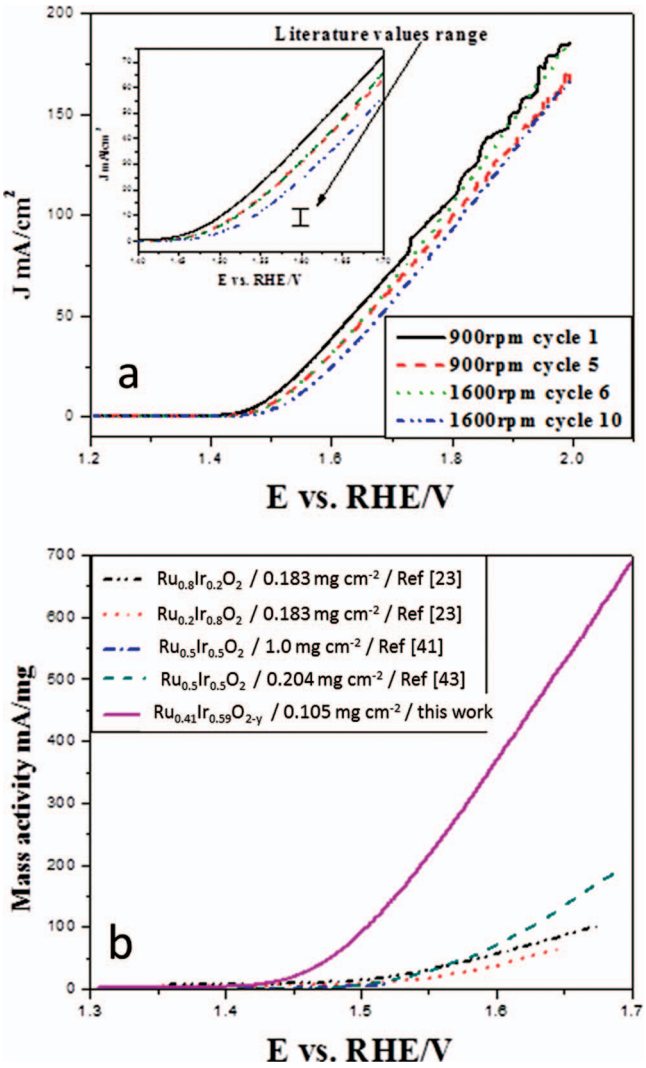

Figure 20. Polarization of the $Ir_xRu_{1-x}O_{2-y}$ film, coated on a Au electrode, into potentials for oxygen evolution in a 0.5 M H_2SO_4 electrolyte a) with rotation rates of 900 and 1600 rpm and b) comparison with literature values normalized to the metal oxide mass.

measured at 1.6 V. The O_2 evolution current density measured by: Owe et al. (10 mA/cm^2); Mamaca et al. (8–12 mA/cm^2); and Mayousse et al. (10–12 mA/cm^2) indicate that the 25–40 mA/cm^2 we observed is very promising.[23,41,43] When normalized to the catalyst mass, shown in Fig. 20b, 400 mA/mg of current is generated compared to the 50–75 mA/mg found in the literature. A mass activity of this level implies full utilization of the metal oxide in the film layer and indicates that most of the active sites throughout are the film accessible.

Conclusions

The results of our work can be summarized as follows:

- Thin crystalline films of $Ir_xRu_{1-x}O_{2-y}$ and $Ir_xPt_{1-x}O_{2-y}$ have been deposited by a proposed mechanism of ballistic nanoparticle accumulation; most particles (mass weighted) are 2-3 nm in diameter but a sizeable (number count) are well below 5 Å.
- Initial film growth, due to the incoming particles, is concentrated in areas of previous particle adherence; this imparts an inherent microporosity as the film grows.
- Aggregation of nanoparticles appears to progress with increasing collection time (i.e., aggregation is absent in the shorter collection times) suggesting a short residence time in the flame and an attraction due to interaction with the surface particles.
- A sizeable portion of the Pt was not incorporated into the crystal structure of the desired $Ir_xPt_{1-x}O_{2-y}$ and this explains the dissolution of the film during polarization; the difference in boiling/melting points are proposed as a reason for the lack of alloying.
- Ir and Ru form a solid solution of $Ir_xRu_{1-x}O_{2-y;}$ the resultant film has remarkable activity toward oxygen evolution.

Ballistic nanoparticle impingement is proposed as a hypothesis for the mechanism of film formation; a mechanism involving some fraction of film growth directly from the vapor phase cannot be ruled out. Electron microscopy suggests that the film formation begins from individual nanoparticles of 2.2–2.5 nm in diameter while the HAADF images, Fig 11, clearly show a preponderance of $Ir_xRu_{1-x}O_{2-y}$ atoms in the early stages of coalesence. There is some evidence that the surface of the 'as-deposited' $Ir_xRu_{1-x}O_{2-y}$ film is enriched in Ir, suggesting some form of surface segregation. A grazing incidence diffraction scan with concomitant XPS of both the unheated film and a film subjected to cyclic polarization would help to better understand this observation. The broad and not very well defined peaks in cyclic voltammetry indicate a variety of Ru/Ir active sites with different formal potentials. The onset potential for oxygen evolution begins around 1.45 V and the current (25–40 mA/cm^2) generated at 1.6 V is double of those reported in the literature. Normalized to the mass of platinum group metal oxides the mass activity is 400 mA/mg$_{metal\text{-}oxide}$ compared to values of 50–75 mA/mg$_{metal\text{-}oxide}$ from literature values.[23,41,43] This represents a significant improvement in performance over traditional film formation strategies (i.e., ink or vacuum based processes) and highlights a path forward in development of a flame based deposition method for the $Ir_xRu_{1-x}O_{2-y}$ system. This work raises further questions about the relationship between film thickness and mass activity; durability; and process options available to optimally tailor the microstructure. Further work will also look at strategies for dispersing the catalyst directly onto a Nafion membrane for CCM manufacture.

Acknowledgments

The authors would like to respectively thank the University of Connecticut Department of Chemical Material and Biomolecular Engineering and the NSF Department of Education GAANN Fellowship for financial support of this work. In addition, the machine shop services of Mark Drobney (UConn) in Technical Services are greatly appreciated. Use of the electron microcopy facilities by David Bell at the Harvard Center for Nanoscale Systems is greatly appreciated. Heng Zhang at UConn's Institute for Material Science is also acknowledged for helpful XPS advice.

References

1. M. A Hickner, H. Ghassemi, Y. S. Kim, B. R. Einsla, and J. E. McGrath, *Chem. Rev.*, **104**, 4587 (2004).
2. C. Heitner-Wirguin, *J. Membr. Sci.*, **120**, 1 (1996).
3. S. A. Grigoriev, V. I. Porembsky, and V. N. Fateev, *Int. J. Hydrogen. Energ.*, **31**, 171 (2006).
4. J. A. Turner, *Science*, **305**, 972 (2004).
5. U. Sahaym and M. Norton, *J. Mater. Sci.*, **43**, 5395 (2008).
6. P. Millet, R. Ngameni, S. A. Grigoriev, and V. N. Fateev, *Int. J. Hydrogen. Energ.*, **36**, 4156 (2011).
7. E. Rasten, G. Hagen, and R. Tunold, *Electrochim. Acta*, **48**, 3945 (2003).
8. J. Rossmeisl, Z. Qu, H. Zhu, G. Kroes, and J. K. Nøskov, *J. Electroanal. Chem.*, **607**, 83 (2007).
9. O. Teschke, *J. Appl. Electrochem.*, **12**, 219 (1982).
10. D. Ginley and D. Cahen, *Fundamentals of Materials for Energy and Environmental Sustainability*, 1st ed., p. 668, Cambridge University Press, New York (2012).
11. D. Das and T. N. Veziroğlu, *Int. J. Hydrogen. Energ.*, **26**, 13 (2001).
12. J. Rossmeisl, Z. Qu, H. Zhu, G. Kroes, and J. K. Nøskov, *J. Electroanal. Chem.*, **607**, 83 (2007).
13. J. Suntivich, K. J. May, H. A. Gasteiger, J. B. Goodenough, and Y. A. Shao-Horn, *Science*, **334**, 1383 (2011).
14. M. H. Miles, E. A. Klaus, B. P. Gunn, J. R. Locker, W. E. Serafin, and S. Srinivasan, *Electrochim. Acta*, **23**, 521 (1978).
15. S. Trasatti, *Electrochim. Acta*, **45**, 2377 (2000).
16. S. Song, H. Zhang, X. Ma, Z. Shao, R. T. Baker, and B. Yi, *Int. J. Hydrogen. Energ.*, **33**, 4955 (2008).
17. E. Antolini and J. Perez, *J. Mater. Sci.*, **46**, 4435 (2011).
18. Y. Wang, D. P. Wilkinson, and J. Zhang, *Chem. Rev.*, **111**, 7625 (2011).
19. Y. Shao, J. Liu, Y. Wang, and Y. Lin, *J. Mater. Chem.*, **19**, 46 (2009).
20. E. Antolini and E. R. Gonzalez, *Solid State Ionics*, **180**, 746 (2009).
21. S. Shrestha, Y. Liu, and W. E. Mustain, *Cataly. Rev.*, **53**, 256 (2011).
22. A. Rabis, P. Rodriguez, and T. J. Schmidt, *ACS Catal.*, **2**, 864 (2012).
23. N. Mamaca, E. Mayousse, S. Arrii-Clacens, T. W. Napporn, K. Servat, N. Guillet, and K. B. Kokoh, *Appl. Catal. B-Environ.*, **111–112**, 376 (2012).
24. F. Kong, S. Zhang, G. Yin, Z. Wang, C. Du, G. Chen, and N. Zhang, *Int. J. Hydrogen Energ.*, **37**, 59 (2012).
25. P. W. T. Lu and S. Srinivasan, *J. Appl. Electrochem.*, **9**, 269 (1979).
26. M. Vuković, *Electrochim. Acta*, **34**, 287 (1989).
27. C. Iwakura, K. Hirao, and H. Tamura, *Electrochim. Acta*, **22**, 335 (1977).
28. R. Kötz and S. Stucki, *Electrochim. Acta*, **31**, 1311 (1986).
29. J. Cheng, H. Zhang, G. Chen, and Y. Zhang, *Electrochim. Acta*, **54**, 6250 (2009).
30. C. L. McDaniel and S. J. Schneider, *J. Res. Nat. Bur. Stand.*, **73A**, 213 (1968).
31. R. Hutchings, K. Müller, R. Kötz, and S. Stucki, *J. Mater. Sci.*, **19**, 3987 (1984).
32. T. R. Ralph, S. Hudson, and D. P. Wilkinson, *ECS Trans.*, **1**, 67 (2006).
33. J. Bett, N. Cipollini, T. Jarvi, and R. Breault, inventors; UTC Fuel Cells LLC, assignee. *Fuel cell having a corrosion resistant and protected cathode catalyst layer*, United States patent US006855453B2. 2005 Feb 15.
34. G. B. Haxel, J. B. Hedrick, and G. J. Orris, *Rare earth elements: critical resources for high technology* [internet]. U.S. Geological Society Fact Sheet 087-02; 2002 [cited 2012 Oct 1]. Available from: http://pubs.usgs.gov/fs/2002/fs087-02/.
35. S. Massari and M. Ruberti, *Resour. Policy*, **38**(1), 36 (2013).
36. T. Ioroi, N. Kitazawa, K. Yasuda, Y. Yamamoto, and H. Takenaka, *J. Electrochem. Soc.*, **147**, 2018 (2000).
37. J. Roller, R. Neagu, F. Orfino, and R. Maric, *J. Mater. Sci.*, **47**, 4604 (2012).
38. R. Maric, J. Roller, and R. Neagu, *J. Therm. Spray Techn.*, **20**, 696 (2011).
39. E. Slavcheva, I. Radev, S. Bliznakov, G. Topalov, P. Andreev, and E. Budevski, *Electrochim. Acta*, **52**, 3889 (2007).
40. K. M. Papazisi, A. Siokou, S. Balomenou, and D. Tsiplakides, *Int. J. Hydrogen Energ.*, **37**(21), 16642 (2012).
41. E. Mayousse, F. Maillard, F. Fouda-Onana, O. Sicardy, and N. Guillet, *Int. J. Hydrogen Energ.*, **36**, 10474 (2011).
42. F. Kong, S. Zhang, G. Yin, N. Zhang, Z. Wang, and C. Du, *Electrochem. Commun.*, **14**, 63 (2012).
43. L. Owe, M. Tsypkin, K. S. Wallwork, R. G. Haverkamp, and S. Sunde, *Electrochim. Acta*, **70**, 158 (2012).
44. Y. E. Roginskaya, T. V. Varlamova, M. D. Goldstein, I. D. Belova, B. S. Galyamov, R. R. Shifrina, V. A. Shepelin, and V. N. Fateev, *Mater. Chem. Phys.*, **30**, 101 (1991).
45. C. B. Carter and M. G. Norton, *Ceramic Materials: Science and Engineering*. 2nd ed., p. 494, Springer, New York (2007).
46. K. Zweibel, *Solar Energy Mater. Solar Cells*, **59**, 1 (1999).
47. V. Mehta and J. S. Cooper, *J. Power Sources*, **114**, 32 (2003).
48. K. C. Neyerlin, G. Bugosh, R. Forgie, Z. Liu, and P. Strasser, *J. Electrochem. Soc.*, **156**, B363 (2009).
49. G. Chen, S. R. Bare, and T. E. Mallouk, *J. Electrochem. Soc.*, **149**, A1092 (2002).
50. J. Roller, *Low platinum electrodes for proton exchange fuel cells manufactured by reactive spray deposition technology* [dissertation]. Vancouver (BC): University of British Columbia (2009).
51. Y. E. Roginskaya and O. V. Morozova, *Electrochim. Acta*, **40**, 817 (1995).

52. R. Maric, R. Neagu, Y. Zhang-Steenwinkel, F. P. F. van Berkel, and B. Rietveld, *J. Power Sources*, **195**, 8198 (2010).
53. R. Nédélec, R. Neagu, S. Uhlenbruck, R. Maric, D. Sebold, H. Buchkremer, and D. Stöver, *Surf. Coat. Tech.*, **205**, 3999 (2011).
54. K. Fatih, R. Neagu, V. Alazate, V. Neburchilov, R. Maric, and W. Haijiang, *ECS Trans.*, **25**, 1177 (2009).
55. R. Maric, J. M. Roller, R. Neagu, K. Fatih, and A. Tuck, *ECS Trans.*, **12**, 59 (2008).
56. J. M. Roller, J. Arellano-Jiméneza, R. Jain, R. Maric, and C. B. Carter, *Activity and Microstructure of Oxygen Evolution Anodes Prepared by a Direct Dry Deposition Technique* [abstract]. 221st ECS meeting; 2012 May 6–10; Seattle, WA.
57. R. Maric, in *PEM Fuel Cell Electrocatalysts and Catalyst Layers: Fundamentals and Applications*, J. Zhang, Editor, p. 917, Springer, London (2008).
58. R. Maric, S. Seward, P. W. Faguy, and M. Oljaca, *Electrochem. Solid St.*, **6**, A91 (2003).
59. M. Kühner and G. Voll, *Carbon Black: Science and Technology*, p. 6, Marcel Dekker, Inc., New York (1993).
60. A. Scott, *Carbon black sales to exceed 11 million m.t. in 2013* [internet]. IHS Chemical Week; 2012 Mar 30 [cited: 2012 Oct 1]. Available from: http://www.chemweek.com/markets/specialty_chemicals/rubber_processing_chemicals/25149.html.
61. W. J. Stark and S. E. Pratsinis, *Powder Technol.*, **126**, 103 (2002).
62. P. Roth, *P. Combust. Inst.*, **31**, 1773 (2007).
63. R. Strobel and S. E. Pratsinis, *J. Mater. Chem.*, **17**, 4743 (2007).
64. M. S. Wooldridge, *Prog. Energ. Combust.*, **24**, 63 (1998).
65. S. E. Pratsinis, in *Aerosol Science and Technology: History and Reviews*, D. S. Ensor, Editor, p. 281–304, RTI International, Research Triangle Park (2011).
66. D. E. Rosner, *Ind. Eng. Chem. Res.*, **44**, 6045 (2005).
67. R. Axelbaum, S. Sastry, D. Dufaux, and C. Frey, *Metal Mater. Trans. B*, **28**, 1199 (1997).
68. H. Zhao, X. Liu, and S. Tse, *J. Nanopart. Res.*, **10**, 907 (2008).
69. K. Wegner, B. Schimmoeller, B. Thiebaut, C. Fernandez, and T. Rao, *Kona*, **29**, 251 (2011).
70. A. Hunt, W. B. Carter, and J. K. Cochran, *Appl. Phys. Lett.*, **63**, 266 (1993).
71. M. Oljaca, Y. Xing, C. Lovelace, S. Shanmugham, and A. Hunt, *J. Mater. Sci. Lett.*, **21**, 621 (2002).
72. J. M. Roller, R. Neagu, Z. Xie, and R. Maric, *Multilayered and gradient electrodes for proton exchange membrane fuel cells by reactive spray deposition technology* [abstract]. 217th ECS meeting; 2010 Apr 25–30; Vancouver, CA.
73. J. M. Roller, R. Neagu, R. Maric, and Z. Xie, *Low platinum electrodes for proton exchange fuel cells manufactured by reactive spray deposition technology* [abstract]. 216th ECS meeting; 2009 Oct 4–9; Vienna, AT.
74. J. Roller, R. Maric, R. Neagu, and F. Orfino. in *FuelCell 2011: Proceedings of the ASME 2011 9th Fuel Cell Science, Engineering and Technology Conference*, p. 277, Aug 7-10 (2011), Washington, DC, USA.
75. S. Litster and G. McLean, *J. Power Sources*, **130**, 61 (2004).
76. R. N. Grass and W. J. Stark, *J. Nanopart. Res.*, **8**, 729 (2006).
77. E. K. Athanassiou, R. N. Grass, and W. J. Stark, *Nanotechnology*, **17**, 1668 (2006).
78. L. Mädler, H. K. Kammler, R. Mueller, and S. E. Pratsinis, *J. Aerosol. Sci.*, **33**, 369 (2002).
79. A. Camenzind, W. R. Caseri, and S. E. Pratsinis, *Nano Today*, **5**, 48 (2010).
80. T. Kodas and M. Hampden-Smith, *Aerosol Processing of Materials*, 1st ed., p. 86, Wiley-VCH, New York (1999).
81. K. Wegner and S. E. Pratsinis, *AIChE J.*, **49**, 1667 (2003).
82. D. B. Williams and C. B. Carter, *Transmission Electron Microscopy: A Textbook for Materials Science*, 1st ed. p. 173, Springer, New York (2008).
83. Y. Li, L. Zhang, Z. Tian, T. Yuan, J. Wang, B. Yang, and F. Qi, *Energ. Fuel*, **23**, 1473 (2009).
84. S. A. Skeen, G. Yablonsky, and R. L. Axelbaum, *Combust. Flame*, **156**, 2145 (2009).
85. C. Poole, *Gas Chromatography*. 1st ed., p. 235, Elsevier, Oxford (2012).
86. K. M. Papazisi, A. Siokou, S. Balomenou, and D. Tsiplakides, *Int. J. Hydrogen Energ.*, **37**(21), 16642 (2013).
87. Z. Zhang and M. G. Lagally, *Science*, **276**, 377 (1997).
88. Z. H. Barber, *J. Mater. Chem.*, **16**, 334 (2006).
89. I. M. Kodintsev, S. Trasatti, M. Rubel, A. Wieckowski, and N. Kaufher, *Langmuir*, **8**, 283 (1992).
90. C. Wagner, W. Riggs, L. Davis, J. Moulder, and G. Mullenberg, *Handbook of X-Ray Photoelectron Spectroscopy*. Perkin Elmer Corporation, Eden Prairie (1978).
91. D. Labou, E. Slavcheva, U. Schnakenberg, and S. Neophytides, *J. Power Sources*, **185**, 1073 (2008).
92. L. D. Burke and D. P. Whelan, *J. Electroanal. Chem.*, **162**, 121 (1984).
93. A. Teleki, R. Wengeler, L. Wengeler, H. Nirschl, and S. E. Pratsinis, *Powder Technol.*, **181**, 292 (2008).
94. S. Tsantilis and S. E. Pratsinis, *Langmuir*, **20**, 5933 (2004).
95. K. Sasaki, M. Shao, and R. Adzic, in *Polymer Electrolyte Fuel Cell Durability*, F. N. Büchi, M. Inaba, and T. J. Schmidt, p. 7, Springer, London (2009).